Tellus (1988), *40B*, 81–115

Atmospheric carbon dioxide measurements in the remote global troposphere, 1981–1984

By T. J. CONWAY,[1] P. TANS,[2] L. S. WATERMAN,[1] K. W. THONING,[2] K. A. MASARIE[2] and R. H. GAMMON,[3] [1] *Air Resources Laboratory, National Oceanic and Atmospheric Administration, Boulder, CO 80303, USA,* [2] *Cooperative Institute for Research in Environmental Sciences, University of Colorado, Boulder, CO 80309, USA,* [3] *Pacific Marine Environmental Laboratory, National Oceanic and Atmospheric Administration, Seattle, WA 98155, USA*

(Manuscript received 26 January; in final form 8 July 1987)

ABSTRACT

The carbon dioxide concentration has been measured in air samples collected approximately once per week at 22 globally distributed sites during 1981–84. All samples were analyzed on the same non-dispersive infrared analyzer apparatus at the NOAA/GMCC laboratory in Boulder. The measured concentrations are directly traceable to the WMO primary CO_2 standards. Samples which do not contain well-mixed, regionally representative air or which have been contaminated during or subsequent to sampling, have been identified. The selected data have been analyzed using an objective curve fitting method which enables improved estimation of uncertainties associated with derived parameters. The latitudinal distribution of annual mean CO_2 concentration at the network sites shows significant interannual variability possibly related to the 1982–83 El Niño/Southern Oscillation event. No evidence was found for significant interannual variations or trends in the phase or amplitude of the seasonal cycle. Significant interannual and interstation variability in the CO_2 growth rate was observed. A growth rate minimum during 1982 was followed by a growth rate maximum in 1983, in association with the intense 1982–83 ENSO event. The mean global growth rate for 1981–84 was 1.22 ppm yr^{-1}.

1. Introduction

The increasing concentration of carbon dioxide in the atmosphere due primarily to fossil fuel combustion is an established feature of the modern global environment (see, for example, Keeling et al., 1976a, 1976b; Pearman and Beardsmore, 1984; Komhyr et al., 1985a). Within the next 50 to 100 years, the effects of this increase on global climate, vegetation, and sea level may produce conditions which will seriously disrupt existing social and economic systems (DOE, 1985a, 1985b, 1985c; EPA, 1983). The magnitude and timing of the environmental changes will depend in part on the rate of increase of CO_2 and other radiatively active trace gases, such as methane and the chlorofluorocarbons (Ramanathan et al., 1985).

To project future CO_2 levels, it is necessary to quantify the anthropogenic source and the natural sources and sinks of CO_2. The primary anthropogenic source through 1984 is known from fossil fuel production data (Rotty, 1983, 1987), but the projection of future emissions is subject to great uncertainty (Edmonds and Reilly, 1985). Quantifying the natural sources and sinks is also difficult because the complex exchanges of carbon in the atmosphere–ocean–biosphere system are variable in both space and time. Several studies of the global carbon cycle have used computer models to simulate the sources, sinks

This paper was presented at the CACGP/IAMAP Conference on *Atmospheric Carbon Dioxide, its Sources, Sinks and Global Transport*, in Kandersteg, Switzerland, September 2–6, 1985. Other papers from this meeting were published in a special issue of *Tellus* (*39B*: 1–2).

and fluxes of carbon. The principal test of a model's accuracy is its ability to reproduce measured features of the atmospheric CO_2 distribution which have not been used to "tune" the model. Model output parameters have included the latitudinal variation of annual mean concentration, the latitudinal dependence of seasonality, the global secular increase, and even the actual time dependent concentration at a specific location (Fraser et al., 1983; Pearman et al., 1983; Oeschger and Heimann, 1983; Fung et al., 1983; M. Heimann, C. D. Keeling and C. J. Tucker, personal communication; Pearman and Hyson, 1986).

The Geophysical Monitoring for Climatic Change (GMCC) program of the National Oceanic and Atmospheric Administration (NOAA) collects air samples from a global network to determine the distribution of CO_2 in the atmospheric boundary layer. These measurements can be used as constraints on models of the global carbon cycle. This program and the data through 1982 have been described by Komhyr et al. (1985a). In this paper we present the measurement results from 1983 and 1984, together with the previous results from 1981 and 1982. The 1981–84 measurements comprise a homogeneous data set in that the methods of sample collection and analysis were essentially unchanged over this period. Also, inclusion of the 1981 and 1982 data allows an examination of the atmospheric CO_2 concentration preceding, during, and following the 1982–83 El Niño/Southern Oscillation (ENSO) event.

Various methods of data selection and curve fitting have been used to calculate the parameters of interest from CO_2 time series data (Keeling et al., 1976a, 1976b; Cleveland et al., 1983; Pearman and Beardsmore, 1984; Bacastow et al., 1985; Komhyr et al., 1985a). In this work, we have used a new objective statistical method of smoothing the data which has allowed us to better estimate the statistical uncertainties associated with derived parameters due to random noise in the data. Although we have used the 1981–82 data as presented by Komhyr et al. (1985a), this new smoothing method has been applied to the 1981–84 record. This leads to differences in the results, e.g., monthly means and seasonal cycle amplitudes, between this work and Komhyr et al. (1985a) for the 1981–82 period. The smoothing used here is an improvement over previous methods. We have not applied it to the entire GMCC record as further improvements are likely. The purpose of this paper is to present our current best estimate of the global CO_2 response to the 1982–83 ENSO event.

2. Experimental

The samples used in this work were collected at 22 sites of the NOAA/GMCC flask sampling network, Table 1 and Fig. 1. The three letter station codes given in Table 1 will be used throughout this paper when referring to the sites. A description of the network from its inception in 1968 through the end of 1982 was given by Komhyr et al. (1985a). Since 1982 fine tuning of the network has continued with the deletion of some sampling sites and the addition of others.

The sample collection procedures have been described in detail by Komhyr et al. (1985a) and Steele et al. (1987), so only a brief review is given here. For part of 1981, samples were collected by hand aspiration of air into previously evacuated flasks. A sample consisted of two flasks collected several minutes apart. During 1981, a new sampling method was introduced and has been in use since then. In this method, two flasks previously filled with a dry gas of known CO_2 concentration and connected in series, are flushed for 5 min at ~ 5 l min^{-1} with ambient air and pressurized to 1.2–1.5 times ambient atmospheric pressure. The portable sampling apparatus includes a 2-m long intake line and a battery-powered electrical pump containing Parel diaphragms and Mylar reed valves. The air is not dried during sample collection.

The cylindrically shaped 0.5 l Pyrex glass flasks taper at both ends to ground glass stopcocks lubricated with Apiezon-N grease. An exception to this is CHR where samples were initially collected in spherical evacuated 5 l greased stopcock flasks which were later replaced by cylindrical evacuated 3 l flasks fitted with one O-ring type stopcock. Samples are collected in evacuated flasks by opening the stopcock and allowing the flask to fill to ambient atmospheric pressure.

The samples are generally collected once per

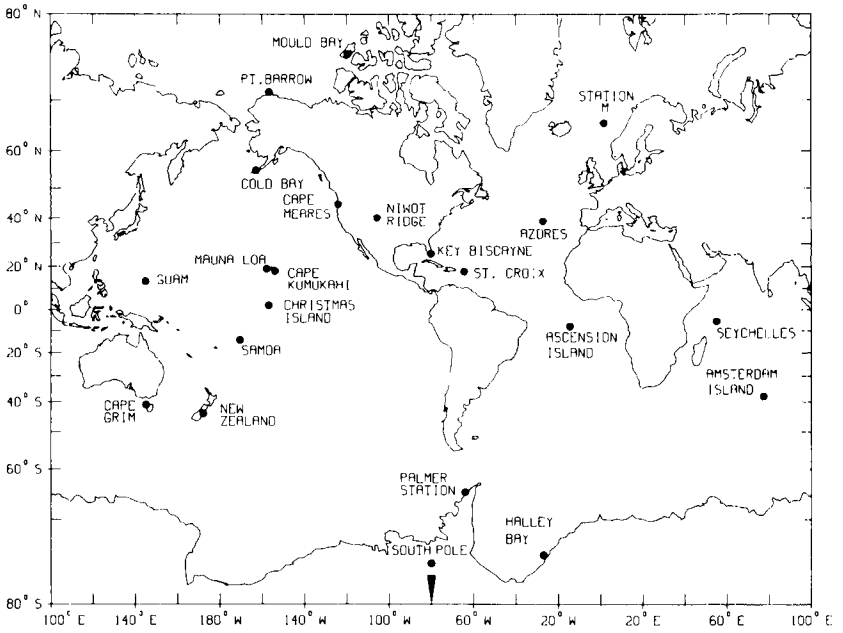

Fig. 1. Locations of the sampling sites in the NOAA/GMCC flask sampling network.

week on a schedule determined largely by the sample collector. The sample collectors have been given guidelines concerning preferred wind speeds, wind directions, and time of day for sample collection when these can be identified for a given site. However, various logistical considerations such as work schedules and access to vehicles often are the factors controlling the day and time of sample collection. To improve the chances of obtaining samples that meet our criterion of being regionally representative background air, we have attempted to choose sampling sites which have a high probability of sampling well-mixed air, uninfluenced by local sources and sinks of CO_2. Therefore most of the sampling sites are remote, marine locations (Fig. 1).

The flask samples are analyzed for CO_2 concentration at the GMCC laboratory in Boulder, using the semiautomatic nondispersive infrared (NDIR) flask analysis apparatus described by Komhyr et al. (1983). The apparatus was modified in August, 1983 when the original gas transfer pump was replaced with a new version. Results of extensive tests showed that the new transfer pump did not remove small amounts of CO_2 as did the original pump (Komhyr et al., 1985a).

The system of standards used by GMCC to determine CO_2 concentrations has been described by Komhyr et al. (1985b) and Thoning et al. (1987). The concentration values assigned to the standard gases are traceable to the primary standards maintained by the World Meteorological Organization (WMO) Central CO_2 Laboratory (CCL) operated by C. D. Keeling at the Scripps Institution of Oceanography. The data reported here in parts per million by volume (ppm) are based on manometric calibrations of the GMCC standards performed at the CCL in 1982. This scale was referred to as the "SIO 1982 manometric scale" in Komhyr et al. (1985a) but it is generally known as the SIO X83 mole fraction scale (C. D. Keeling, personal communication). Recent work at the CCL has resulted in the X85 mole fraction scale. For data obtained prior to 1985 there is very little (<0.1 ppm) difference between the X83 and X85 scales.

Table 1. *Summary of flask sampling sites*

Site code	Site	Country	Latitude	Longitude	Elevation* (meters)	Cooperating agency	Site type
AMS	Amsterdam Is., Indian Ocean	France	37°52′S	77°32′E	150	Centre des Faibles Radioactivities	Island seashore
ASC	Ascension Is., S. Atlantic	U.K.	7°55′S	14°25′W	54	U.S.A.F., Pan American World Airways	Island seashore
AVI	St. Croix, Virgin Islands	U.S. Territory	17°45′N	64°45′W	3	Fairleigh Dickinson University	Island seashore
AZR	Azores (Terceira Is.) N. Atlantic	Portugal	38°45′N	27°05′W	30	U.S.A.F./7th Weather Wing	Island seashore
BRW	Point Barrow, Alaska	U.S.	71°19′N	156°36′W	11	GMCC Station	Arctic coastal seashore
CBA	Cold Bay, Alaska	U.S.	55°12′N	162°43′W	25	NOAA/National Weather Service	Treeless peninsula
CGO	Cape Grim, Tasmania	Australia	40°41′S	144°41′E	94	CSIRO, Division of Atmospheric Research	Promontory seashore
CHR	Christmas Island	Kiribati	2°00′N	157°18′W	3	Scripps Inst. of Oceanography	Island seashore
CMO	Cape Meares, Oregon	U.S.	45°29′N	124°00′W	30	Oregon Graduate Center	Promontory seashore
GMI	Guam (Marianas Is.), North Pacific	U.S. Territory	13°26′N	144°47′E	2	University of Guam	Island seashore
HBA	Halley Bay	Antarctica	75°40′S	27°00′W	3	British Antarctic Survey	Barren seashore
KEY	Key Biscayne, Florida	U.S.	25°40′N	80°10′W	3	NOAA/Sea-Air-Interaction Laboratory	Coastal island seashore
KUM	Cape Kumukahi, Hawaii	U.S.	19°31′N	154°49′W	3	GMCC Site	Island seashore
MBC	Mould Bay, N.W.T.	Canada	76°14′N	119°20′W	15	Environment Canada/Atmospheric Environment Service	Island tundra
MLO	Mauna Loa, Hawaii	U.S.	19°32′N	155°35′W	3397	GMCC Station	Barren volcanic mountain slope
NWR	Niwot Ridge, Colorado	U.S.	40°03′N	105°38′W	3749	Univ. of Colorado/INSTAAR	Alpine mountain
NZL	Kaitorete Spit, New Zealand	New Zealand	43°50′S	172°38′W	3	U.S. National Center for Atmos. Research	Treeless spit
PSA	Palmer Station (Anvers Is.)	Antarctica	64°55′S	64°00′W	33	Washington State Univ. Lab. for Atmospheric Research	Barren island seashore
SEY	Seychelles (Mahé Is.) Indian Ocean	Seychelles	4°40′S	55°10′E	3	N.M. State Univ./Physical Science Lab.	Island seashore
SMO	American Samoa, S. Pacific	U.S. Territory	14°15′S	170°34′W	42	GMCC Station	Island rocky promontory
SPO	Amundsen Scott (South Pole)	Antarctica	89°59′S	24°48′W	2810	GMCC Station/National Science Foundation	Ice and snow covered plateau
STM	Ocean Station "M"	N. Atlantic	66°00′N	2°00′E	6	Norway Meteorological Institute	Open ocean

* Elevation above mean sea level.

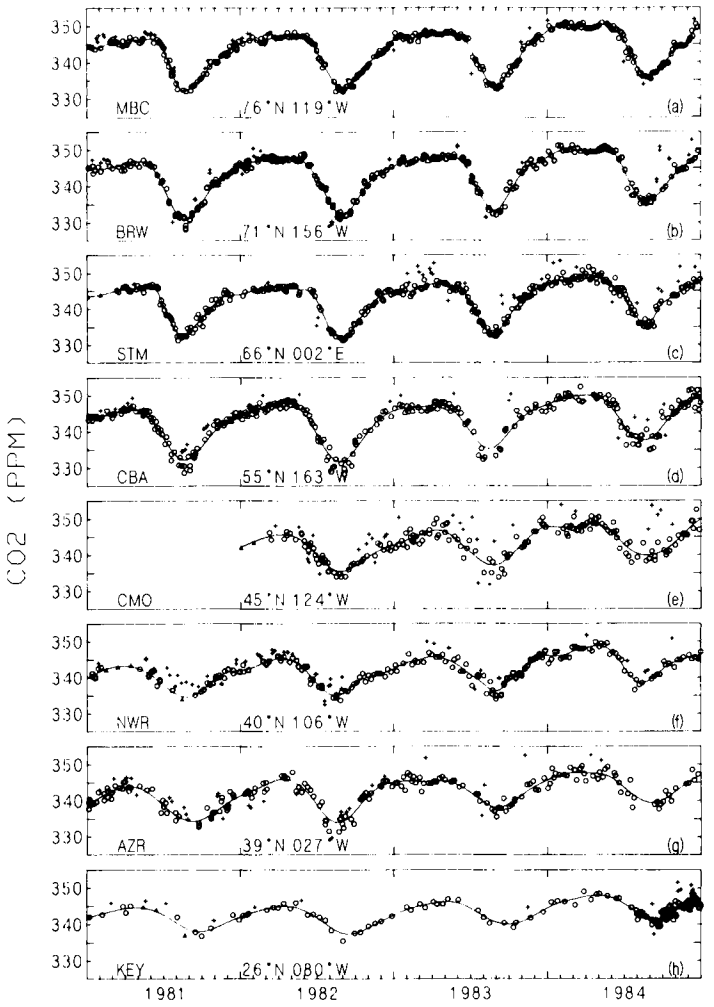

Fig. 2. Results of flask sample CO_2 measurements from 1981–84. Circles indicate samples collected in air believed to be well-mixed and regionally representative. The values plotted are pair averages or individual measurements in the case of retained single samples. Crosses indicate samples flagged as not representative of background conditions. Triangles indicate interpolated or extrapolated points used by Komhyr et al. (1985a) to constrain the curve fits. The solid lines are cubic spline fits to the selected data following the method described in the text.

3. Results

The flask sample measurement results are shown in Fig. 2(a–v). The plots are arranged in order by latitude, starting with MBC at 76° N, to facilitate comparison of sites and to emphasize the variability of CO_2 concentration with latitude.

3.1. Data selection

Flask sampling is an economical way of acquiring CO_2 concentration measurements from a network of remote sites. The interpretation of these data requires consideration of many factors other than natural atmospheric variability which may affect the CO_2 concentration of the sampled air. These factors include errors in collection technique by the sample taker; stopcock failure following sample collection with subsequent contamination of the sample; and the influence of local anthropogenic sources and biospheric sources and sinks of CO_2. Since the purpose of

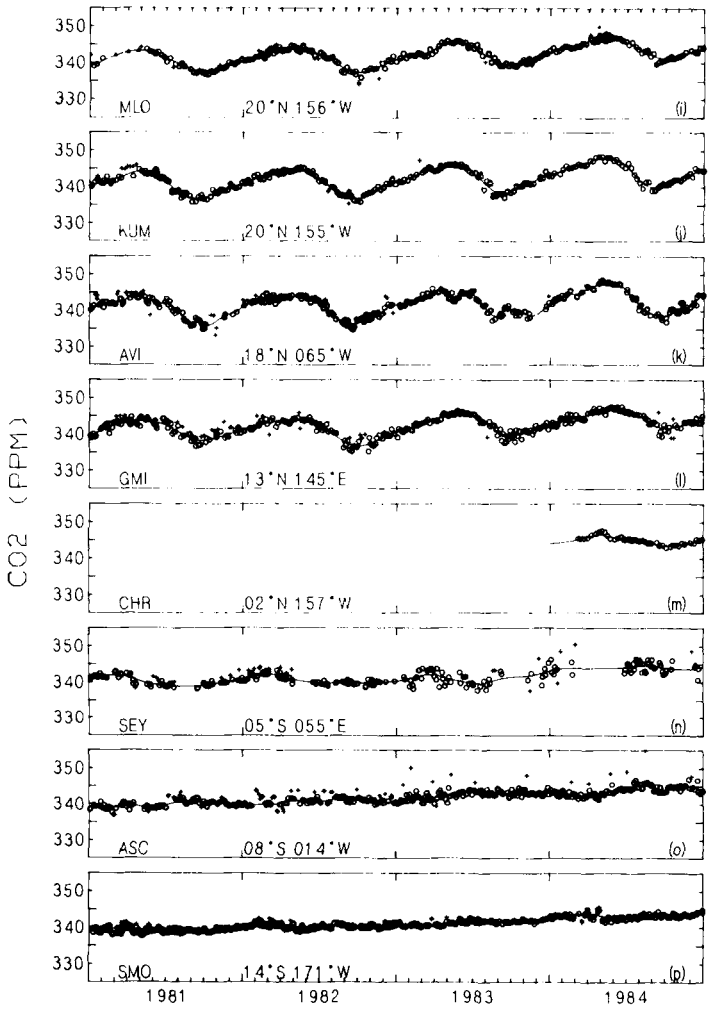

Fig. 2 (continued)

these measurements is to determine the CO_2 concentration of well-mixed regionally representative air, it is necessary to examine the data carefully and reject or flag contaminated samples and samples affected by local sources or sinks.

The data presented here from 1981 and 1982 were analyzed previously and we use the selected data as reported by Komhyr et al. (1985a). For the 1983 and 1984 data we used a similar selection scheme, described below.

First, since tests have shown that flask samples collected as pairs using the methods described above have nearly identical CO_2 concentrations, we examined the agreement between members of sample pairs. The distribution of pair differences for 1981 through 1984 shows that 62% of the pairs agree to within 0.25 ppm and 77% agree to within 0.50 ppm (Fig. 3). The distribution has a long tail and differences greater than 10 ppm have been collapsed into the last cell in Fig. 3. Based on this distribution, we have chosen a cutoff point for acceptable samples at 0.50 ppm. When the CO_2 concentrations in the two flasks differ by more than 0.50 ppm it is probable that an error in sampling or stopcock failure has occurred resulting in contamination of one or both flasks. Since contamination with room air or air affected by other anthropogenic sources usually increases the CO_2 concentration, the high member of such a pair is rejected. The low

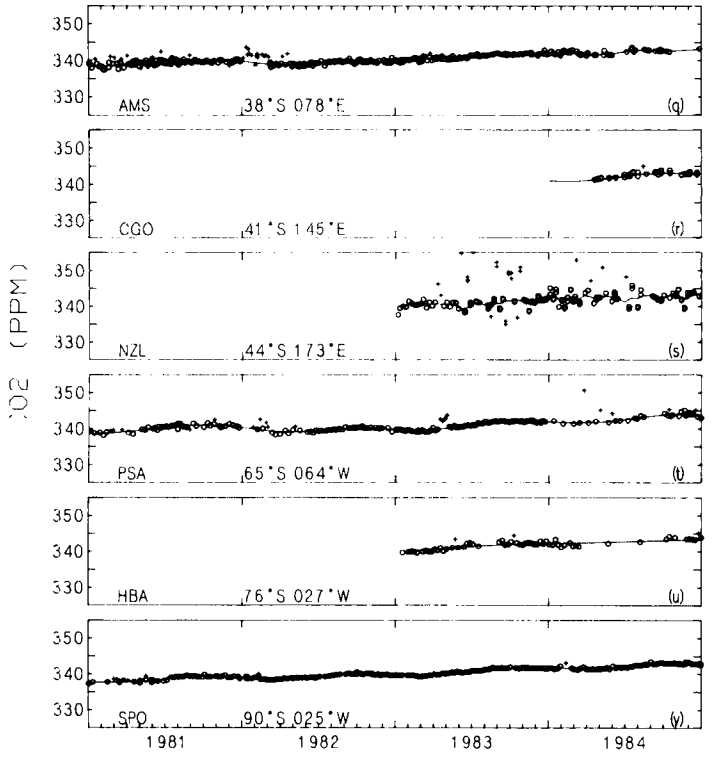

Fig. 2 (continued)

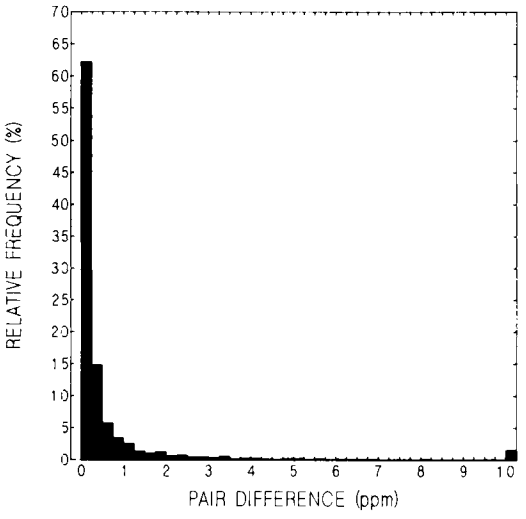

Fig. 3. Frequency distribution of CO_2 concentration differences for flask sample pairs. All differences greater than 10 ppm are collapsed into the last cell.

member of the pair is flagged as being suspect and will be reconsidered after curve fitting as described below.

Next, sample pairs which differ by less than 0.50 ppm, but which are clearly the result of incorrect sample collection are rejected. This decision may be based on comments noted by the sample taker on the data sheet indicating incomplete flushing of flasks or suspected contamination from some local source, possibly the sample taker himself. In other cases the measured concentration itself, either extremely high or low, is an indication of incorrect sampling. It is important that we reject clear outliers before fitting a curve. The curve fits are based on least squares procedures and outliers would receive an inordinate amount of weight.

After the clearly defective values have been rejected, the data are examined for samples which appear to be valid measurements, but which are inconsistent with the bulk of the data.

These samples are flagged as being not representative of background conditions at the site. This decision is often based on the wind speed or direction at the time of sampling combined with information concerning the location of sources and sinks near the sampling site. In some cases the decision is based only on the discrepancy between the sample and the general trend of the data. These samples, which are flagged somewhat subjectively, are also reexamined after the curve fitting.

The retained sample pairs are averaged to give a single value and a cubic spline function, described in detail below, is fitted to these values plus the low members of pairs with poor agreement and any other retained single flasks. The samples flagged as not representative of background conditions are not included in this fit. The final selected data set is obtained by re-examining the data with respect to the fitted curve and the residual standard deviation (RSD) of the points from the curve. Values falling within ± 3*RSD of the curve are retained with no flag. If a point was previously flagged but falls within this envelope, the flag is removed. If a point was not flagged but falls outside this envelope, it is flagged as being not representative of background conditions. Low members of pairs with poor agreement which were initially retained, but which fall outside ± 3*RSD are rejected.

As mentioned earlier, this selection scheme was applied to the 1983–84 data while the selected data of Komhyr et al. (1985a) were used for 1981–82. The selection scheme described above rejects fewer marginal points than the method of Komhyr et al. (1985a). Examination of the data indicates that the difference in selection schemes produces no significant difference in the estimated amplitudes of the seasonal cycles or the monthly and annual mean concentrations.

The plots in Fig. 2 show the fitted curves and the selected data. The flagged values are included in the plots since they may be valid samples containing information concerning the CO_2 concentration or variability at a site resulting from local or non-background influences. In this paper we are concerned with the distribution and variability of CO_2 concentration in the remote, well-mixed, global troposphere, so it is necessary to remove these local effects which are difficult to interpret based on the information available. Samples rejected for poor pair agreement and obvious sampling errors are not shown in the plots. For 1983 and 1984, 80% of the data have been retained as measurements of regionally representative, well-mixed air; 10% are rejected due to poor pair agreement; 4% are rejected due to sampling errors; and 6% are flagged as not representing background conditions.

The first few months of 1984 for CHR and CGO have been extrapolated to enable calculation of annual means. These extrapolations are based on comparisons to NZL for CGO and unpublished SIO data for CHR (C. D. Keeling, personal communication).

The NOAA/GMCC flask data have been archived with WMO and the Carbon Dioxide Information Center (CDIC) at Oak Ridge National Laboratory, Oak Ridge, Tennessee. The data archived with WMO are pair averages with flags distinguishing the categories of our selection scheme. The CDIC archive contains a complete listing of individual flask values with flags indicating the results of our data selection.

3.2. Curve fitting

The analysis of CO_2 data typically requires fitting some type of curve to the data. The reasons for curve fitting are: (1) to aid in data selection and determination of the scatter or noise in the atmospheric signal at each site, (2) to interpolate through missing or unevenly spaced data so that estimates of monthly, seasonal, or annual values are weighted properly, (3) to smooth the data so that estimates of parameters such as the amplitude and phase of the annual cycle are not dependent on variations occurring over short (5–10 day) time scales, and (4) to provide an analytic or at least continuous function representing the variation of CO_2 concentration with time which can be manipulated mathematically to determine trends or from which parameterized signals can be separated.

Curve fitting methods which have been used by different investigators are a least squares fit to an oscillating power function (Keeling et al., 1976a, 1976b); removal of an average seasonal cycle followed by a least squares fit to a cubic spline with knots every 12 months to determine the long-term trend (Komhyr et al., 1985a); non-linear digital filters to separate components with specific frequencies (Cleveland et al., 1983); a least squares

fit to a combination of an exponential long-term trend, a four-harmonic seasonality, and a smoothing cubic spline to the residuals (Bacastow et al., 1985; Keeling et al., 1985); and the removal of the seasonal signal determined by the complex demodulation technique followed by smoothing of the residuals with low-pass filters (Thompson et al., 1986).

While much useful information has been gained from these techniques, they also have drawbacks. The cubic spline with knots every 12 months is subject to end effects and possible phase shifts (Enting, 1986). Also, the use of cubic splines is not completely objective because the knot spacing, or the spline stiffness, in the case of smoothing splines, can be adjusted until the curve is judged (usually by eye) to be a satisfactory fit. The imposition of a parameterized seasonality or long-term trend, whether an analytical function or an average determined from several years of data, may result in poor fitting where the record departs from the specified form and may not be appropriate for sites where the seasonality is not yet well characterized. This is especially true when the parameterized form determined for one location is applied to another location (Keeling et al., 1976a, 1976b). The complex demodulation technique requires that the record be extended by one year at the beginning and end, which is not appropriate for short records.

The method used to obtain the curves in Fig. 2 is a modification (M. Manning, personal communication) of the smoothing spline (program SMOOTH) presented by de Boor (1978). This algorithm finds the piecewise cubic polynomial function f that minimizes the expression:

$$p \sum_{i=1}^{N} \left\{ \frac{y(i) - f(x(i))}{Dy(i)} \right\}^2 + (1-p) \int_{x_1}^{x_n} \{ f''(t) \}^2 \, dt, \tag{1}$$

where $y(i)$ are the data points at times $x(i)$ and $Dy(i)$ are weights assigned to the data proportional to their uncertainty. The parameter p determines whether the fit pays more attention to minimizing the distance from the data, resulting in more and sharper curves, or to minimizing its own second derivative, resulting in a smoother curve. The problem is to objectively assign a value to p, rather than varying p until the curve is judged by eye to be a "good" fit.

M. Manning proposed that p be modified until the residuals $y(i) - f(x(i))$ meet a statistical criterion, namely the runs test. The runs test counts the number of sign changes in the series of consecutive (time ordered) residuals and compares that to the number expected for a time series of random numbers, in our case half the number of observations. If p is large, the number of sign changes is close to the number of observations as the curve attempts to reach each data point. If p is too small, $f(t)$ will be too stiff and there will be few sign changes. Our assumption is that the noise does not exhibit serial correlation (has no "memory"). Therefore, when the residuals meet the runs test, we have effected a separation of signal from noise that we believe to be close to optimal.

Once the curve fits had been obtained, the residuals were further analyzed for their statistical

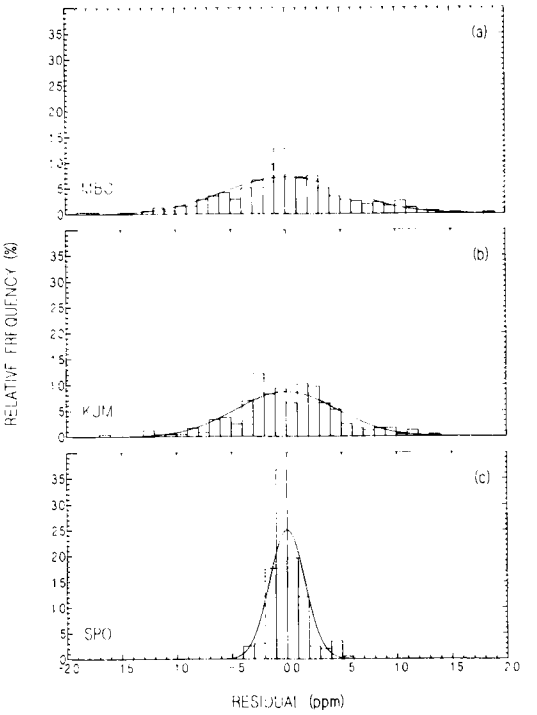

Fig. 4. Frequency distributions of the residuals from the cubic spline curves for MBC, KUM, and SPO. The smooth curves are normal distributions with mean = 0 and σ = RSD for each site. The residuals for MBC and KUM are normally distributed while the distribution for SPO is positively skewed and more sharply peaked than a normal distribution.

Table 2. *Curve fit parameters and analysis of residuals*

Site	RSD (ppm)	$Dy(i)$ (ppm)	N	r_1	r_2	r_3	$\overline{D}$ (rms) (ppm)	N_{eff}	$\bar{f}$ (wk^{-1})	T_{eff} (wk)	P	T'_{eff} (wk)	σ_{RM} (ppm)
AMS	0.39	0.16	304	−0.05	0.03	−0.22	0.12	10.4	1.5	6.9	0.981	7.4	0.04
ASC	0.64	0.11	324	−0.02	−0.17	−0.20	0.23	7.7	1.6	4.8	0.994	4.5	0.07
AVI	0.58	0.13	372	0.09	−0.33	−0.15	0.28	4.3	1.8	2.4	0.999	2.9	0.06
AZR	1.35	0.16	194	−0.01	−0.07	0.00	0.58	5.4	0.9	6.0	0.973	9.1	0.20
BRW	0.85	0.06	207	−0.04	−0.15	−0.02	0.56	2.3	1.0	2.3	0.966	6.0	0.12
CBA	1.39	0.11	281	0.20	0.06	0.19	0.58	5.7	1.4	4.1	0.933	8.7	0.16
CGO	0.40	0.11	37	0.04	−0.09	−0.25	0.22	3.3	1.2	2.8	0.670		
CHR	0.38	0.15	51	0.48	0.25	0.06	0.28	1.8	1.3	1.4	0.982		
CMO	1.56	0.11	168	−0.07	0.01	0.11	0.77	4.1	1.1	3.7	0.908		0.21
GMI	0.78	0.12	320	−0.03	0.03	−0.11	0.31	6.3	1.5	4.2	0.957	7.8	0.09
HBA	0.41	0.12	55	−0.05	−0.37	0.07	0.21	3.8	0.5	7.6	0.786	9.6	0.08
KEY	1.02	0.10	141	0.11	−0.02	−0.07	0.60	2.9	0.7	4.1	0.946	9.3	0.17
KUM	0.46	0.11	246	−0.16	−0.33	−0.08	0.27	2.9	1.2	2.4	0.999	2.9	0.06
MBC	0.57	0.09	323	−0.14	−0.30	−0.17	0.33	3.0	1.6	1.9	0.999	2.5	0.06
MLO	0.51	0.06	198	−0.06	−0.09	−0.14	0.23	4.9	1.0	4.9	0.903	7.9	0.07
NWR	0.93	0.11	208	−0.01	−0.19	−0.15	0.48	3.8	1.0	3.8	0.991	5.5	0.13
NZL	0.98	0.11	143	0.09	−0.42	−0.19	0.55	3.2	1.4	2.3	0.999		0.11
PSA	0.34	0.12	164	0.06	−0.06	0.00	0.15	5.2	0.8	6.5	0.718	15.9	0.05
SEY	1.05	0.16	204	0.06	0.01	0.03	0.42	6.3	1.0	6.3	0.967	9.5	0.15
SMO	0.49	0.12	279	0.17	−0.04	−0.13	0.21	5.4	1.3	4.2	0.978	6.8	0.06
SPO	0.16	0.08	199	−0.24	−0.29	−0.02	0.08	4.0	1.0	4.0	0.990	5.0	0.02
STM	0.87	0.08	317	−0.10	−0.16	−0.15	0.41	4.5	1.5	3.0	0.993	4.1	0.10

properties. The serial correlation coefficients at lags 1 through 3, r_1, r_2, and r_3 are not significant (Table 2). Thus, we can indeed consider the residuals as mutually independent and the method is self consistent in this regard. Histograms of the residual distributions were constructed which suggested that the residuals were distributed normally with mean = 0 and σ = RSD. The distributions for MBC, KUM, and SPO are shown as examples in Fig. 4.

The Kolmogorov-Smirnov goodness of fit test showed that, for all sites but SPO, the residual distributions are normal. The distribution for SPO is positively skewed (more points above the best fit curve than below, Fig. 2(v)) and is more sharply peaked than a normal distribution. That we end up with normal distributions is, of course, partly due to the initial selection procedure. Wtihout selection the distributions would look somewhat normal, but with very long tails.

The curve fit parameters and the results of the statistical analysis of the residual series for each site are given in Table 2. The residual standard deviation is an output of the program and we interpret it as a measure of the scatter due to real atmospheric variability at each site. It is much larger than the values we assigned to $Dy(i)$. At each site we made $Dy(i)$ an estimate of the analytical precision of the measurements by calculating the average pair difference, $\overline{DF}$, between members of sample pairs for the four years and setting $Dy(i) = \overline{DF}/(2)^{\frac{1}{2}}$ for all i. This turned out to be of no importance because, as long as all $Dy(i)$ are equal, assigning a value amounts to scaling the parameter p. For different $Dy(i)$ the algorithm will find a different numerical value of p that corresponds to the same amount of smoothing.

From this analysis, we concluded that the best fit curves produced by this modified smoothing cubic spline have picked up the signal present in the data and that the residuals are independent

Table 3—*footnote*

The values in the columns labelled Data and σ_d are the means and sample standard deviations calculated directly from the flask sample data. The number of data points used is in the column labelled N. The mean values and statistical uncertainties calculated from the best fit curves, as described in the text, are in the columns labelled Spline and σ_s.

Table 3. *Monthly and annual mean atmospheric CO_2 concentration in ppm above 300 ppm*

	AMS					ASC					AVI				
	Data	σ_d	N	Spline	σ_s	Data	σ_d	N	Spline	σ_s	Data	σ_d	N	Spline	σ_s
1981 Jan	38.6	0.4	7	38.5	0.2	39.5	0.8	5	39.3	0.2	41.2	0.7	6	41.3	0.2
Feb	38.3	0.9	5	38.4	0.2	38.8	0.6	7	39.0	0.2	41.9	0.5	8	41.9	0.2
Mar	38.6	0.8	5	38.7	0.2	39.7	0.7	6	39.4	0.2	42.4	0.8	5	42.6	0.3
Apr	39.2	0.5	11	39.1	0.1	39.6	0.8	5	39.6	0.2	43.9	0.5	7	43.9	0.2
May	39.6	0.4	6	39.4	0.2	39.0	0.4	5	39.1	0.2	43.2	1.0	6	43.1	0.2
Jun	39.5	0.6	9	39.5	0.2	39.2	0.3	7	39.2	0.2	41.8	0.7	5	42.0	0.3
Jul	39.7	0.6	11	39.6	0.1	40.4	1.3	3	40.1	0.3	40.9	1.4	8	40.8	0.2
Aug	39.6	0.5	7	39.7	0.2	40.7	0.7	5	40.9	0.2	37.4	1.3	5	37.7	0.3
Sep	39.7	0.3	8	39.7	0.2	40.9	0.7	8	40.8	0.2	36.7	1.1	8	36.6	0.2
Oct	39.7	0.2	8	39.7	0.2	40.2	0.5	6	40.3	0.2	35.6	0.7	3	36.2	0.4
Nov	39.9	0.4	5	39.8	0.2	40.3	0.6	8	40.2	0.2	38.7	0.4	4	38.2	0.3
Dec	39.9	0.3	10	39.8	0.2	39.7	0.4	7	39.8	0.2	39.2	0.4	2	39.8	0.4
Annual	39.4	0.6	92	39.35	0.05	39.8	0.7	72	39.82	0.06	40.2	2.7	67	40.33	0.07
1982 Jan	39.0		1	39.6	0.4	39.7	0.3	7	39.7	0.2	42.1	0.4	8	42.1	0.2
Feb				39.2		40.0	0.4	3	39.8	0.3	43.3	0.9	13	43.1	0.2
Mar	38.8	0.4	7	38.9	0.1	40.0	0.3	4	40.1	0.2	43.1	0.7	18	43.1	0.1
Apr	38.9	0.3	5	38.8	0.2	41.0	0.8	4	40.7	0.2	43.8	0.3	12	43.8	0.2
May	38.8	0.3	8	38.8	0.1	41.0	0.6	4	41.0	0.2	44.0	0.4	12	43.9	0.2
Jun	39.1	0.3	10	39.1	0.1	41.0	0.6	8	40.9	0.2	43.0	0.4	16	43.1	0.1
Jul	39.5	0.5	6	39.4	0.1	40.4	0.2	3	41.0	0.3	40.7	1.1	15	40.7	0.1
Aug	39.8	0.2	7	39.7	0.1	42.0	0.2	7	41.6	0.2	37.3	0.9	10	37.5	0.2
Sep	39.7	0.4	9	39.8	0.1	41.1	0.5	7	41.4	0.2	36.1	0.9	14	36.2	0.1
Oct	39.9	0.4	8	39.8	0.1	41.4	0.4	8	41.2	0.2	37.9	0.6	14	37.7	0.1
Nov	39.8	0.3	7	39.7	0.1	40.7	0.5	7	40.8	0.2	39.0	0.6	8	39.1	0.2
Dec	39.8	0.5	9	39.8	0.1	40.6	0.3	4	40.6	0.2	41.4	0.4	4	41.2	0.3
Annual	39.4	0.5	77	39.38	0.04	40.7	0.7	66	40.73	0.06	41.0	2.8	144	40.94	0.05
1983 Jan	39.9	0.3	9	40.0	0.1	41.2	1.0	8	41.2	0.3	41.9	0.6	9	41.8	0.2
Feb	40.2	0.5	7	40.2	0.1	42.1	1.0	6	41.9	0.3	43.2	0.7	7	43.0	0.2
Mar	40.5	0.6	6	40.5	0.1	41.4	1.1	8	41.8	0.3	44.6	0.9	8	44.7	0.2
Apr	40.7	0.3	8	40.6	0.1	42.5	0.9	7	42.2	0.3	45.4	0.5	7	45.2	0.2
May	40.6	0.4	7	40.7	0.1	42.5	1.2	8	42.6	0.3	43.6	0.8	9	43.8	0.2
Jun	40.9	0.3	8	41.0	0.1	43.2	0.6	7	43.2	0.3	45.0	0.5	9	44.8	0.2
Jul	41.4	0.2	8	41.3	0.1	43.4	0.5	8	43.4	0.3	42.3	0.9	6	42.5	0.2
Aug	41.6	0.3	7	41.6	0.1	43.3	0.8	9	43.2	0.3	39.0	1.1	7	39.0	0.2
Sep	41.8	0.2	6	41.8	0.1	43.0	0.7	7	43.2	0.3	40.1	1.2	7	40.1	0.2
Oct	41.7	0.2	6	41.8	0.1	43.4	0.9	9	43.2	0.3	39.6	0.5	7	39.6	0.2
Nov	42.0	0.3	4	41.9	0.2	43.1	0.5	7	43.2	0.3	38.8	0.9	4	38.9	0.3
Dec	41.9	0.4	9	42.0	0.1	43.1	0.7	9	43.1	0.3	41.4	0.9	3	40.5	0.3
Annual	41.1	0.7	85	41.11	0.04	42.7	0.8	93	42.67	0.08	42.1	2.3	83	41.97	0.06
1984 Jan	41.9	0.4	7	42.1	0.1	43.0	0.7	8	43.0	0.3	43.1	0.7	9	43.1	0.2
Feb	42.5	0.3	6	42.1	0.2	42.5	0.6	7	42.5	0.3	44.9	0.5	4	44.5	0.3
Mar	41.7	0.4	8	41.9	0.1	42.0	0.5	8	42.2	0.3	45.1	1.3	6	45.1	0.3
Apr	41.6	0.3	5	41.6	0.2	42.3	0.9	7	42.3	0.3	47.1	1.0	6	46.8	0.3
May	41.7	0.5	6	41.7	0.2	43.2	0.9	8	43.1	0.3	47.7	0.4	7	47.7	0.2
Jun				42.1		43.8	0.3	7	43.9	0.3	46.6	1.0	6	46.7	0.3
Jul	42.8	0.5	5	42.6	0.2	44.9	1.1	8	44.7	0.3	42.4	1.5	6	43.3	0.3
Aug	42.8	0.1	4	42.8	0.2	45.2	0.7	8	45.1	0.3	39.9	1.0	6	39.8	0.3
Sep	42.7	0.2	6	42.7	0.2	43.7	0.6	8	44.1	0.3	38.4	0.7	4	38.4	0.3
Oct	42.4	0.1	2	42.6	0.3	44.4	0.6	9	44.3	0.2	39.4	1.3	8	39.5	0.2
Nov				42.7		44.9	0.9	8	44.9	0.3	40.8	1.0	9	40.8	0.2
Dec	43.2		1	43.0	0.4	44.1	1.3	7	44.4	0.3	43.3	1.3	7	43.1	0.2
Annual	42.3	0.6	50	42.33	0.05	43.7	1.1	93	43.71	0.07	43.2	3.1	78	43.22	0.07

Table 3—*continued*

	AZR					BRW					CBA				
	Data	σ_d	N	Spline	σ_s	Data	σ_d	N	Spline	σ_s	Data	σ_d	N	Spline	σ_s
1981 Jan	39.7	1.3	8	40.1	0.4	44.9	0.5	2	44.9	0.6	43.9	0.4	9	44.0	0.4
Feb	41.8	1.2	8	41.9	0.4				45.0		44.8	0.8	5	44.8	0.5
Mar	44.3	0.9	5	43.4	0.6	45.5	0.5	3	45.7	0.5	45.4	0.5	5	45.7	0.5
Apr	43.4	0.6	3	43.8	0.7	46.7	0.6	2	46.8	0.6	46.4	0.6	5	46.2	0.5
May	43.5	0.8	2	42.8	0.9	46.2	0.2	3	46.6	0.5	45.2	0.7	9	45.0	0.4
Jun	39.7	2.8	4	40.2	0.6	43.5	2.0	3	43.1	0.5	41.5	1.6	8	41.1	0.4
Jul	37.2	1.8	5	37.2	0.6	33.7	2.6	2	36.2	0.6	35.5	2.4	6	35.7	0.4
Aug	35.8		1	35.0	1.3	31.0	1.9	4	31.4	0.4	31.2	1.7	6	32.5	0.4
Sep	33.3	0.5	3	34.5	0.7	33.0	2.0	4	33.0	0.4	32.9	2.2	7	33.9	0.4
Oct	36.5	1.2	5	35.8	0.6	38.7	2.5	3	38.2	0.5	39.9	2.0	3	38.2	0.6
Nov	38.7	1.6	5	38.2	0.6	42.1	0.9	6	42.2	0.3	42.4	0.8	8	41.9	0.4
Dec	40.4	1.9	5	40.4	0.6	44.9	0.9	5	44.6	0.4	44.3	0.9	7	44.0	0.4
Annual	39.5	3.4	54	39.41	0.17	40.9	5.8	37	41.44	0.13	41.1	5.2	78	41.04	0.12
1982 Jan	41.8	0.7	5	42.1	0.7	45.9	0.9	6	46.2	0.3	45.4	1.3	8	45.4	0.5
Feb	43.3	1.2	4	43.6	0.7	47.8	0.5	3	47.4	0.4	46.1	1.1	8	46.4	0.5
Mar	44.1	1.3	2	45.2	1.0	47.8	0.4	6	47.8	0.3	47.3	0.6	8	47.4	0.5
Apr	46.6	0.4	4	45.9	0.7	47.5	0.3	4	47.7	0.4	47.9	0.9	9	48.0	0.5
May	44.2	2.6	4	44.6	0.7	47.6	0.7	5	47.5	0.3	47.4	1.0	6	46.7	0.6
Jun	43.2	1.6	4	41.2	0.7	44.1	2.0	4	44.9	0.4	43.7	1.8	6	42.4	0.6
Jul	35.4	3.1	6	36.7	0.6	39.2	1.7	5	39.1	0.3	36.0	2.5	7	36.3	0.5
Aug	33.8	1.7	4	34.2	0.7	32.3	1.4	4	33.5	0.4	30.7	1.3	5	32.2	0.6
Sep	34.2	1.4	4	35.5	0.7	33.4	1.8	4	33.2	0.4	32.6	3.2	9	33.0	0.5
Oct	41.1	0.7	5	39.2	0.7	39.2	2.2	5	37.9	0.3	38.5	1.9	3	37.4	0.8
Nov	42.2	1.8	3	42.7	0.8	42.9	0.7	3	42.3	0.4	42.5	1.6	4	41.9	0.7
Dec	44.8	0.9	5	44.6	0.7	44.2	1.0	4	44.7	0.4	44.8	1.1	4	44.9	0.7
Annual	41.2	4.3	50	41.26	0.21	42.7	5.5	53	42.65	0.10	41.9	6.0	77	41.79	0.15
1983 Jan	44.6	1.4	5	45.3	0.5	46.7	1.0	3	46.3	0.6	46.8	0.9	5	46.3	0.6
Feb	46.3	1.2	5	45.4	0.5	46.8	0.5	3	47.0	0.6	46.4	0.7	5	46.7	0.6
Mar	44.6	1.4	5	45.3	0.5	47.6	0.5	4	47.5	0.5	46.0	0.3	4	47.1	0.7
Apr	45.8	0.7	4	45.4	0.6	48.0	0.4	7	48.0	0.4	47.7	0.7	9	47.4	0.5
May	45.4	0.3	4	45.0	0.6	48.0	0.3	6	48.1	0.4	46.5	0.7	5	46.2	0.6
Jun	43.9	0.3	2	43.4	0.9	46.9	0.7	4	46.1	0.5	43.8	2.0	5	42.5	0.6
Jul	41.1	1.1	3	41.0	0.7	40.1	2.2	4	40.0	0.5	35.3	3.4	4	37.8	0.7
Aug	38.1	1.1	3	38.8	0.7	33.3	1.3	2	34.4	0.7	33.2	0.3	2	35.6	1.0
Sep	37.9	1.8	5	38.4	0.5	34.4	2.7	5	35.1	0.4	37.9	3.1	4	37.7	0.7
Oct	39.8	1.1	5	40.2	0.5	41.1	2.1	4	40.7	0.5	43.9	1.8	4	41.8	0.7
Nov	44.9	0.5	3	42.7	0.7	45.5	1.4	5	45.1	0.4	45.8	0.6	2	45.0	1.0
Dec	44.0	1.9	3	44.8	0.7	46.4	1.1	4	47.2	0.5	46.3	0.9	4	46.8	0.7
Annual	43.0	3.0	47	42.96	0.18	43.7	5.3	51	43.77	0.14	43.3	5.0	53	43.37	0.20
1984 Jan	46.2	2.0	6	46.4	0.6	49.3	1.6	6	49.0	0.4	47.9	1.4	6	48.1	0.7
Feb	47.6	1.3	3	47.3	0.9	50.1	0.6	5	49.9	0.4	49.7	0.7	5	49.3	0.8
Mar	47.4	1.8	6	47.6	0.6	49.5	0.5	5	49.7	0.4	49.2	1.8	5	49.8	0.8
Apr	46.1	0.6	2	47.4	1.1	49.3	0.2	5	49.6	0.4	49.4	0.5	4	49.7	0.9
May	47.9	1.3	4	46.8	0.8	50.2	0.4	18	50.1	0.2	48.7	1.3	5	48.2	0.8
Jun	45.1	2.4	4	44.8	0.8	48.4	1.2	4	47.4	0.4	45.4	3.0	6	44.2	0.7
Jul	41.3	3.0	4	41.9	0.8	39.8	2.7	5	40.7	0.4	38.2	1.7	6	39.5	0.7
Aug				39.8		35.5	0.6	4	36.1	0.4	37.5	2.0	7	37.6	0.6
Sep	38.8	0.8	4	39.4	0.8	36.0	0.7	2	37.1	0.6	38.6	3.3	7	39.3	0.6
Oct	41.3	1.6	5	40.9	0.7	41.7	3.0	4	41.1	0.4	44.7	1.2	5	43.3	0.8
Nov	44.4		1	43.5	1.6	44.3	0.3	4	44.6	0.4	46.7	1.1	8	46.8	0.6
Dec	46.5	1.7	4	46.5	0.8	47.6	1.5	4	47.7	0.4	49.1	2.1	9	48.8	0.6
Annual	44.8	3.0	43	44.35	0.24	45.1	5.5	66	45.22	0.11	45.4	4.7	73	45.35	0.20

Table 3—*continued*

	CGO					CHR					CMO				
	Data	σ_d	N	Spline	σ_s	Data	σ_d	N	Spline	σ_s	Data	σ_d	N	Spline	σ_s
1981 Jan															
Feb															
Mar															
Apr															
May															
Jun															
Jul															
Aug															
Sep															
Oct															
Nov															
Dec															
Annual															
1982 Jan											42.7	0.9	2	43.1	0.8
Feb														44.4	
Mar											45.3	1.5	2	45.4	0.8
Apr											45.7	0.9	4	45.6	0.6
May											45.0	1.1	4	44.4	0.6
Jun											41.5	1.6	7	41.7	0.4
Jul											37.7	1.6	8	38.3	0.4
Aug											34.5	0.5	5	35.9	0.5
Sep											36.2	1.7	4	36.1	0.6
Oct											38.7	0.9	4	38.1	0.6
Nov											42.0	1.9	3	40.3	0.6
Dec											41.9	0.9	4	42.0	0.6
Annual											41.0	3.8	47	41.26	0.17
1983 Jan											43.3	1.5	6	43.5	0.7
Feb											45.0	1.3	6	44.8	0.7
Mar											45.3	1.5	6	46.0	0.7
Apr											47.4	2.3	5	46.6	0.8
May											46.1	2.2	6	45.3	0.7
Jun											41.7	2.0	4	42.4	0.9
Jul											41.0		1	39.4	1.8
Aug											36.8	2.0	4	37.6	0.9
Sep											37.4	2.9	6	38.2	0.7
Oct											42.5	2.4	3	41.0	1.0
Nov											43.9	1.6	5	44.4	0.8
Dec											48.5	1.3	6	47.0	0.7
Annual											43.2	3.6	58	43.00	0.24
1984 Jan				40.9					44.2		45.9		1	47.7	1.6
Feb				40.8					44.7		46.8	1.1	7	47.6	0.6
Mar				40.9		45.3	0.2	4	45.5	0.2	47.7	1.4	7	47.9	0.6
Apr	41.1	0.1	4	41.1	0.2	46.7	0.4	6	46.4	0.2	48.9	1.2	7	48.3	0.6
May	41.4	0.1	4	41.5	0.2	46.3	0.9	7	46.3	0.1	47.7	1.7	5	47.2	0.7
Jun	41.8	0.4	4	42.0	0.2	45.3	0.4	6	45.5	0.2	45.4	2.7	5	44.4	0.7
Jul	42.7	0.6	6	42.4	0.2	44.8	0.3	7	44.9	0.1	40.6	2.4	5	41.4	0.7
Aug	42.7		1	42.8	0.4	44.3	0.4	5	44.3	0.2	39.8	2.3	4	40.0	0.8
Sep	43.2	0.4	6	43.0	0.2	43.7	0.4	4	43.7	0.2	40.5	2.2	4	40.2	0.8
Oct	43.4	0.6	2	43.1	0.3	43.3	0.4	4	43.4	0.2	41.5	1.6	6	41.9	0.7
Nov	42.7	0.2	6	43.0	0.2	43.7	0.4	3	43.9	0.2	45.3	0.5	7	44.8	0.6
Dec	43.0	0.4	4	42.9	0.2	44.8	0.6	5	44.8	0.2	48.9	2.3	5	48.2	0.7
Annual	42.4	0.8	37	42.03	0.07	44.8	1.1	51	44.79	0.05	44.9	3.4	63	44.96	0.20

Table 3—*continued*

	GMI					HBA					KEY				
	Data	σ_d	N	Spline	σ_s	Data	σ_d	N	Spline	σ_s	Data	σ_d	N	Spline	σ_s
1981 Jan	40.0	1.1	7	40.2	0.3						42.1		1	42.4	1.0
Feb	42.1	0.9	9	42.0	0.3						42.7		1	43.2	1.0
Mar	43.5	0.5	6	43.2	0.4						45.0		1	44.1	1.0
Apr	43.4	0.8	8	43.6	0.3						44.2	1.3	2	44.6	0.7
May	43.9	0.9	6	43.7	0.4						44.8		1	44.4	1.0
Jun	43.2	1.0	8	43.2	0.3						44.0		1	43.4	1.0
Jul	41.9	1.4	8	41.8	0.3									41.6	
Aug	39.8	0.4	4	39.8	0.4						39.5	3.5	2	39.4	0.7
Sep	37.9	0.9	7	38.4	0.3						37.3	0.8	2	38.1	0.7
Oct	39.0	0.8	6	38.6	0.4						39.0		1	38.4	1.0
Nov	39.7	0.8	4	39.6	0.4									39.7	
Dec	41.0	0.7	7	40.6	0.3						41.9	1.0	2	41.3	0.7
Annual	41.3	2.0	80	41.21	0.10						42.1	2.7	14	41.71	0.28
1982 Jan	41.4	0.4	6	41.7	0.3						42.7	0.3	3	42.8	0.4
Feb	43.2	0.7	5	42.8	0.4									43.8	
Mar	43.4	1.0	4	43.4	0.4						44.4	0.4	3	44.7	0.4
Apr	43.6	0.4	8	43.8	0.3						45.1	1.0	2	45.0	0.5
May	44.1	0.3	6	44.0	0.3						45.9		1	44.4	0.7
Jun	43.1	1.2	7	43.2	0.3						42.6	0.1	2	42.9	0.5
Jul	41.7	0.8	6	41.5	0.3						41.6	0.6	2	40.6	0.5
Aug	38.8	1.9	4	39.0	0.4						38.3		1	38.4	0.7
Sep	36.5	0.9	7	37.0	0.3						36.5	1.5	2	37.5	0.5
Oct	37.4	1.6	4	36.9	0.4						37.9		1	38.2	0.7
Nov	38.1	1.3	6	38.3	0.3						39.9	0.6	2	39.8	0.5
Dec	40.2	0.7	7	39.9	0.3						41.5	1.0	2	41.6	0.5
Annual	41.0	2.7	70	40.94	0.10						41.5	3.1	21	41.62	0.16
1983 Jan	41.0	0.8	8	41.2	0.3	39.8	0.1	2	39.7	0.3	44.8		1	43.3	0.7
Feb	42.4	0.9	7	42.4	0.3	39.9	0.2	3	39.9	0.2	43.9		1	44.5	0.7
Mar	43.7	0.4	5	43.6	0.3	40.1	0.2	4	40.2	0.2	45.1	0.8	2	45.4	0.5
Apr	44.8	0.9	7	44.8	0.3	40.5	0.4	4	40.6	0.2	45.8	0.4	3	46.0	0.4
May	45.7	0.5	9	45.7	0.3	41.0	0.2	3	41.1	0.2	47.0		1	46.1	0.7
Jun	45.8	0.3	7	45.6	0.3	42.0	0.6	3	41.6	0.2	46.8		1	45.2	0.7
Jul	44.0	0.8	7	44.2	0.3	41.7	0.4	2	41.9	0.3	43.8		1	43.3	0.7
Aug	42.0	1.3	6	41.9	0.3				42.2		41.1	1.1	2	41.4	0.5
Sep	39.5	1.5	8	40.0	0.3	42.4	0.6	4	42.3	0.2	40.4		1	40.3	0.7
Oct	39.9	1.2	8	40.0	0.3	42.2	0.4	4	42.4	0.2	39.8	1.0	2	40.3	0.5
Nov	41.2	0.8	7	41.0	0.3	42.3	0.2	4	42.3	0.2	41.8		1	41.5	0.7
Dec	42.2	0.7	6	42.1	0.3	42.5	0.5	4	42.2	0.2	43.4		1	43.4	0.7
Annual	42.7	2.1	85	42.71	0.08	41.3	1.1	37	41.36	0.06	43.6	2.4	17	43.39	0.16
1984 Jan	43.1	0.9	9	43.1	0.2	41.9	0.8	5	42.0	0.2	46.1	0.2	2	45.2	0.8
Feb	44.0	1.0	7	44.0	0.3	41.8	0.5	3	41.8	0.3	46.1		1	46.3	1.1
Mar	44.5	0.7	8	44.8	0.3	41.4	0.2	2	41.8	0.3	47.0	2.6	2	47.1	0.8
Apr	46.3	0.5	8	46.0	0.3				41.8		47.2	0.9	2	47.7	0.8
May	46.8	0.6	9	46.8	0.2	42.2		1	42.0	0.5	47.9	0.5	2	47.5	0.8
Jun	46.7	0.6	8	46.7	0.3				42.3		46.9	0.0	2	46.4	0.8
Jul	45.7	0.3	7	45.5	0.3				42.6		43.7	0.8	4	44.2	0.6
Aug	43.6	0.9	6	43.7	0.3	42.6		1	42.9	0.5	42.3	0.7	9	42.0	0.4
Sep	41.5	1.7	6	42.0	0.3				43.2		40.6	1.0	16	41.1	0.3
Oct	41.8	0.8	5	41.7	0.3	43.8	0.4	3	43.4	0.3	43.0	1.5	21	42.6	0.3
Nov	43.1	0.7	5	42.7	0.3	43.4		1	43.6	0.5	44.7	1.3	12	44.6	0.3
Dec	43.8	0.8	7	43.8	0.3	43.4	0.1	2	43.6	0.3	45.6	1.5	16	45.7	0.3
Annual	44.2	1.8	85	44.23	0.08	42.6	0.9	18	42.58	0.11	45.1	2.3	89	45.03	0.12

Table 3—*continued*

	KUM					MBC					MLO				
	Data	σ_d	N	Spline	σ_s	Data	σ_d	N	Spline	σ_s	Data	σ_d	N	Spline	σ_s
1981 Jan	40.7	0.6	4	41.0	0.3	44.2	0.4	4	44.1	0.3	39.0		1	40.0	0.4
Feb	41.8	0.7	4	41.8	0.3	45.2	0.9	3	45.0	0.4				41.5	
Mar	42.3	0.7	2	42.9	0.4	45.4	0.7	7	45.5	0.2				42.6	
Apr	44.8		1	44.4	0.5	46.1	0.9	4	46.0	0.3				43.2	
May	43.8	0.4	4	44.1	0.3	45.9	0.5	4	46.2	0.3	43.4	0.4	2	43.1	0.3
Jun	43.8	0.9	18	43.1	0.1	45.6	0.8	7	45.9	0.2	42.3	0.4	2	41.9	0.3
Jul	39.2	1.2	5	39.5	0.2	38.9	3.0	10	39.2	0.2	39.8	1.0	4	40.3	0.2
Aug	37.5	0.7	11	37.4	0.2	32.4	0.3	3	32.6	0.4	39.3	0.5	8	38.7	0.2
Sep	36.8	0.8	4	36.7	0.3	34.2	1.3	7	34.1	0.2	37.3	0.2	3	37.5	0.3
Oct	37.7	1.2	4	37.8	0.3	38.3	1.7	4	38.2	0.3	37.2	0.5	5	37.5	0.2
Nov	39.3	0.8	5	39.2	0.2	41.4	1.1	8	41.4	0.2	39.1	0.9	3	38.6	0.3
Dec	40.3	0.8	5	40.2	0.2	44.0	1.2	9	44.0	0.2	40.1	0.6	4	39.9	0.2
Annual	40.7	2.7	67	40.64	0.06	41.8	4.8	70	41.81	0.07	39.7	2.1	32	40.39	0.08
1982 Jan	41.4	0.7	7	41.6	0.1	46.0	0.9	3	45.9	0.3	40.9	0.4	5	41.1	0.3
Feb	42.6	0.6	5	42.6	0.2	46.0	0.7	7	46.1	0.2	42.3	0.6	5	42.3	0.3
Mar	44.1	0.4	5	44.0	0.2	46.9	0.2	3	46.6	0.3	44.1	0.3	3	43.4	0.3
Apr	44.4	0.2	7	44.4	0.1	47.3	0.6	5	47.3	0.2	43.8	0.6	6	43.9	0.2
May	45.0	0.5	5	45.0	0.2	47.4	0.4	8	47.4	0.2	43.9	0.4	4	43.8	0.3
Jun	43.0	1.1	4	43.3	0.2	45.7	1.2	9	45.9	0.2	43.2	0.1	2	43.0	0.4
Jul	41.0	0.9	3	40.9	0.2	40.1	1.1	6	39.8	0.2	41.6	0.6	5	41.4	0.3
Aug	38.2	1.0	5	38.3	0.2	33.0	0.8	9	34.0	0.2	39.1	1.7	3	39.3	0.3
Sep	37.0	0.9	4	36.9	0.2	33.6	1.1	8	33.5	0.2	37.6	0.8	4	37.6	0.3
Oct	37.4	1.1	4	37.5	0.2	37.4	1.0	8	37.2	0.2	37.5	1.2	4	37.5	0.3
Nov	39.4	0.6	5	39.5	0.2	41.4	1.5	6	41.2	0.2	38.9	1.0	3	38.8	0.3
Dec	41.3	0.8	4	41.1	0.2	43.9	1.1	8	44.2	0.2	40.3	1.2	5	40.3	0.3
Annual	41.2	2.7	58	41.24	0.05	42.4	5.3	80	42.40	0.06	41.1	2.4	49	41.02	0.08
1983 Jan	42.0	0.6	5	41.9	0.2	47.1	0.5	8	47.0	0.2	41.8	0.6	4	41.6	0.3
Feb	43.5	0.7	3	43.4	0.3	46.6	0.8	7	46.7	0.2	42.3	0.3	4	42.3	0.3
Mar	45.0	0.6	4	44.9	0.3	47.8	0.5	9	47.7	0.2	42.7	0.8	5	43.2	0.2
Apr	45.4	0.6	6	45.5	0.2	47.7	0.2	8	47.7	0.2	45.4	0.7	4	44.8	0.3
May	46.2	0.1	7	46.2	0.2	48.0	0.4	7	47.9	0.2	45.7	0.3	4	45.6	0.3
Jun	44.9	0.9	4	45.1	0.3	46.8	0.4	8	46.4	0.2	45.0	0.7	5	45.0	0.2
Jul	41.9	1.9	4	42.0	0.3	39.8	1.3	6	40.5	0.3	43.5	1.5	3	43.2	0.3
Aug	38.9	1.6	4	39.2	0.3	34.4	1.5	8	34.5	0.2	41.1	1.0	4	41.1	0.3
Sep	38.2	0.8	4	38.2	0.3	34.5	1.6	7	34.9	0.2	39.6	0.4	5	39.7	0.2
Oct	40.6	0.8	8	40.1	0.2	39.3	1.0	8	39.5	0.2	39.8	0.6	4	39.8	0.3
Nov	41.1	0.1	3	41.4	0.3	44.8	0.9	4	44.7	0.3	40.7	0.7	4	40.8	0.3
Dec	43.3	0.8	4	43.1	0.3	46.5	1.0	5	47.1	0.3	42.4	0.7	5	42.3	0.2
Annual	42.6	2.6	56	42.58	0.07	43.6	5.2	85	43.68	0.06	42.5	2.1	51	42.45	0.08
1984 Jan	43.7	0.7	4	43.8	0.2	49.4	0.6	5	49.3	0.3	43.5	0.6	4	43.5	0.3
Feb	45.4	0.3	4	45.3	0.2	50.1	0.5	9	50.1	0.2	44.2	0.2	4	44.2	0.3
Mar	46.0	0.2	4	46.0	0.2	49.8	0.5	7	49.8	0.2	44.8	0.4	4	45.2	0.3
Apr	47.6	0.6	4	47.5	0.2	49.2	0.2	8	49.3	0.2	46.4	0.5	14	46.3	0.1
May	47.7	0.6	5	47.8	0.2	50.1	0.4	5	50.1	0.3	47.0	0.6	12	46.9	0.1
Jun	46.3	1.0	4	46.5	0.2	48.2	1.0	9	48.1	0.2	46.2	0.4	4	46.2	0.3
Jul	43.6	2.2	5	43.7	0.2	42.3	1.8	8	42.4	0.2	44.6	0.8	4	44.6	0.3
Aug	40.3	1.3	4	40.4	0.2	36.3	0.8	8	36.6	0.2	42.7	0.6	5	42.7	0.2
Sep	39.9	0.7	8	40.0	0.2	37.1	1.0	7	37.1	0.2	40.5	0.2	3	41.4	0.3
Oct	41.4	0.6	10	41.4	0.1	41.0	2.2	8	40.9	0.2	41.5	0.3	4	41.4	0.3
Nov	42.7	0.8	8	42.6	0.2	44.3	0.2	8	44.5	0.2	42.6	0.7	4	42.4	0.3
Dec	44.3	0.9	5	44.4	0.2	47.9	1.8	6	48.1	0.3	43.6	0.7	4	43.6	0.3
Annual	44.1	2.7	65	44.09	0.05	45.5	5.1	88	45.48	0.07	44.0	2.0	66	44.01	0.06

Table 3—*continued*

	NWR					NZL					PSA				
	Data	σ_d	N	Spline	σ_s	Data	σ_d	N	Spline	σ_s	Data	σ_d	N	Spline	σ_s
1981 Jan	40.9	1.1	5	40.8	0.4						38.9	0.1	2	38.6	0.3
Feb	42.6	0.5	2	42.5	0.6						38.7	0.6	2	38.8	0.3
Mar	43.0		1	43.2	0.8									39.1	
Apr	43.5		1	43.2	0.8						38.8	0.3	2	39.5	0.3
May	41.2	1.2	3	42.0	0.5						40.0	0.4	3	39.9	0.2
Jun	40.0	1.9	7	39.5	0.3						40.2	0.4	5	40.3	0.2
Jul	36.5		1	36.7	0.8						40.7	0.5	6	40.6	0.2
Aug	34.0		1	34.8	0.8						40.8	0.5	3	40.9	0.2
Sep	35.6	0.7	2	35.3	0.6						40.9	0.5	3	41.0	0.2
Oct	37.9	0.9	7	37.9	0.3						41.3	0.4	3	41.0	0.2
Nov	40.5	0.8	6	40.6	0.3						40.8	0.4	4	40.8	0.2
Dec	41.9	0.5	6	41.9	0.3						40.7	0.3	3	40.5	0.2
Annual	39.8	3.1	42	39.85	0.12						40.2	0.9	36	40.08	0.07
1982 Jan	42.3	0.8	4	42.4	0.4									40.1	
Feb	44.5	0.2	2	43.6	0.5						40.0	0.2	2	39.7	0.2
Mar	44.8	1.0	6	44.9	0.3						38.6	0.3	3	39.4	0.2
Apr	44.9	0.7	5	45.2	0.3						39.3	0.5	3	39.2	0.2
May	43.7	1.3	7	43.8	0.3						39.6		1	39.2	0.3
Jun	41.1	2.1	8	40.4	0.3						39.2	0.3	4	39.4	0.2
Jul	37.5	0.3	4	36.7	0.4						39.5	0.2	5	39.6	0.2
Aug	34.8	0.8	6	35.0	0.3						39.9	0.1	4	39.9	0.2
Sep	37.0	0.9	4	36.7	0.4						40.3	0.1	4	40.1	0.2
Oct	39.7	1.2	4	39.5	0.4						40.4	0.2	5	40.2	0.2
Nov	40.7	0.7	5	40.7	0.3						40.3	0.1	4	40.1	0.2
Dec	41.4	1.1	3	41.6	0.4						39.7	0.8	2	39.9	0.2
Annual	41.0	3.3	58	40.87	0.10						39.7	0.6	37	39.74	0.06
1983 Jan	43.1	1.1	3	43.4	0.7	39.7	1.3	5	39.4	0.3	39.7	0.2	6	39.7	0.1
Feb	44.8	1.3	4	44.6	0.6	40.6	0.2	3	40.8	0.4	39.4	0.2	5	39.6	0.1
Mar	45.9	1.4	3	45.5	0.7	40.7	0.9	5	40.7	0.3	39.6	0.5	5	39.7	0.1
Apr	45.9	0.4	3	45.8	0.7	40.6	0.8	2	40.6	0.5	39.8	0.2	2	40.0	0.2
May	44.1	1.2	3	44.5	0.7	40.5	0.8	5	40.4	0.3	40.6	0.2	5	40.4	0.1
Jun	42.6	2.1	5	42.2	0.5	39.6	1.2	6	39.5	0.3	40.8	0.2	5	40.9	0.1
Jul	39.5	1.6	3	39.6	0.7	41.3	0.2	4	40.9	0.3	41.4	0.3	5	41.4	0.1
Aug	36.5	2.3	7	36.9	0.4	40.7	1.1	7	40.5	0.3	42.0	0.2	6	41.8	0.1
Sep	37.8	2.2	6	37.2	0.5	40.6	1.5	6	41.2	0.3	42.1	0.1	5	42.0	0.1
Oct	40.7	0.6	9	40.5	0.4	41.4	0.2	3	41.7	0.4	42.2	0.0	5	42.1	0.1
Nov	44.1	1.2	7	43.5	0.4	40.8	1.2	14	40.9	0.2	42.2	0.2	7	42.1	0.1
Dec	46.3	0.8	8	45.9	0.4	42.1	0.4	12	42.1	0.2	42.0	0.2	5	42.0	0.1
Annual	42.6	3.3	61	42.46	0.15	40.7	0.7	72	40.71	0.08	41.0	1.1	61	40.99	0.03
1984 Jan	45.5	1.5	5	45.9	0.4	42.5	1.7	9	42.3	0.4	42.1		1	41.8	0.5
Feb	46.1	1.4	4	46.3	0.5	41.8	2.0	8	41.7	0.4	41.3	0.0	2	41.7	0.3
Mar	48.0	0.3	4	47.7	0.5	42.2	1.5	5	42.2	0.6	41.6		1	41.7	0.5
Apr	48.1	1.3	3	48.4	0.5	41.9	1.5	5	42.1	0.6	41.7	0.3	2	41.8	0.3
May	48.4	1.3	5	48.3	0.4	42.0	1.0	5	42.4	0.6	41.7		1	42.0	0.5
Jun	45.8	1.0	4	45.2	0.5	42.7	1.0	4	41.7	0.6	42.2	0.0	2	42.3	0.3
Jul	39.4	2.2	4	40.3	0.5	41.3	2.9	6	41.6	0.5	42.6	0.4	3	42.7	0.3
Aug	38.1	0.4	2	38.5	0.7	43.6	1.1	2	42.7	0.9	43.4	0.3	2	43.1	0.3
Sep	40.3	0.6	4	40.6	0.5	42.1	0.5	8	42.2	0.4				43.5	
Oct	43.5	0.7	4	43.3	0.5	43.0	0.5	5	42.8	0.6	43.8	0.3	4	43.8	0.2
Nov	45.0	0.4	3	44.8	0.5	42.2	2.1	8	42.3	0.4	44.2	0.7	5	43.9	0.2
Dec	45.7	0.9	5	45.7	0.4	43.4	0.5	6	43.2	0.5	43.7	0.7	7	43.8	0.2
Annual	44.5	3.5	47	44.57	0.14	42.4	0.7	71	42.27	0.14	42.6	1.0	30	42.67	0.08

Table 3—*continued*

	SEY					SMO					SPO				
	Data	σ_d	N	Spline	σ_s	Data	σ_d	N	Spline	σ_s	Data	σ_d	N	Spline	σ_s
1981 Jan	41.6	0.4	7	41.6	0.2	39.4	0.5	7	39.5	0.2	37.5	0.3	2	37.6	0.2
Feb	41.3	0.2	4	41.9	0.3	39.7	0.7	6	39.6	0.2	37.7		1	37.7	0.2
Mar	42.4	0.6	7	41.8	0.2	40.0	0.9	8	39.8	0.2	37.6		1	37.6	0.2
Apr	40.7	1.3	5	40.9	0.3	39.4	0.7	6	39.4	0.2	37.8		1	37.8	0.2
May	39.1	0.4	3	39.8	0.3	38.9	0.7	8	39.0	0.2	38.0	0.3	7	37.9	0.1
Jun	39.5	0.7	3	39.2	0.3	38.9	0.4	6	38.9	0.2	38.0	0.0	2	38.1	0.2
Jul	39.1	0.4	6	39.0	0.2	39.1	0.5	10	39.0	0.2	38.8	0.5	3	38.7	0.1
Aug				38.8		39.2	0.4	6	39.1	0.2	39.3	0.2	5	39.3	0.1
Sep	38.8	0.9	3	39.0	0.3	38.9	0.2	4	39.1	0.3	39.3	0.1	4	39.4	0.1
Oct	39.4	0.5	7	39.4	0.2	39.2	0.7	5	39.2	0.2	39.4	0.3	4	39.3	0.1
Nov	39.9	0.2	4	39.9	0.3	39.7	0.3	5	39.5	0.2	39.3	0.2	5	39.3	0.1
Dec	40.6	0.4	4	40.5	0.3	39.6	0.3	6	39.7	0.2	39.1	0.3	4	39.1	0.1
Annual	40.2	1.2	53	40.13	0.08	39.3	0.4	77	39.31	0.06	38.5	0.8	39	38.48	0.03
1982 Jan	41.3	0.9	6	41.3	0.2	40.2	0.3	10	40.3	0.2	38.9	0.3	5	38.9	0.1
Feb	42.1	0.8	7	42.1	0.2	41.1	0.9	6	41.0	0.2	38.4	0.0	3	38.6	0.1
Mar	42.4	0.8	6	42.1	0.2	41.2	0.3	6	41.0	0.2	38.4	0.1	4	38.4	0.1
Apr	40.9	0.7	7	41.3	0.2	40.4	0.8	9	40.4	0.2	38.7	0.2	4	38.7	0.1
May				40.4		39.4	0.6	8	39.7	0.2	38.9	0.1	5	38.9	0.1
Jun	39.9	0.3	4	40.0	0.3	39.9	0.4	8	39.9	0.2	39.0	0.1	4	39.0	0.1
Jul	39.6	0.6	5	39.8	0.3	40.2	0.5	10	40.3	0.2	39.4	0.1	4	39.3	0.1
Aug	39.9	0.2	4	39.8	0.3	40.8	0.3	5	40.4	0.2	39.8	0.1	3	39.8	0.1
Sep	39.9	0.5	8	39.8	0.2	40.0	0.1	3	40.3	0.3	40.0	0.1	4	40.1	0.1
Oct	39.4	1.2	3	39.8	0.4	40.1	0.3	5	40.2	0.2	40.1	0.2	6	40.1	0.1
Nov	40.0	0.6	7	39.9	0.2	40.3	0.2	4	40.3	0.3	39.8	0.2	7	39.9	0.1
Dec	40.2	0.1	2	40.1	0.4	40.6	0.4	6	40.6	0.2	39.8	0.1	4	39.7	0.1
Annual	40.5	1.0	59	40.51	0.08	40.4	0.5	80	40.35	0.06	39.3	0.6	53	39.28	0.02
1983 Jan	40.4	1.4	3	40.6	0.9	40.7	0.6	6	40.7	0.2	39.6	0.1	4	39.6	0.1
Feb	41.0	1.8	8	41.4	0.5	40.7	0.4	8	40.7	0.1	39.5	0.2	4	39.5	0.1
Mar	43.3	0.7	7	42.2	0.6	40.6	0.1	4	40.6	0.2	39.5	0.1	4	39.5	0.1
Apr	40.8	1.9	7	41.6	0.6	40.7	0.5	10	40.7	0.1	40.0	0.2	4	39.9	0.1
May	41.4	1.4	3	40.7	0.9	41.5	0.6	8	41.3	0.1	40.5	0.2	4	40.4	0.1
Jun	40.1	1.2	6	40.0	0.6	41.9	0.6	8	41.9	0.1	40.5	0.1	4	40.6	0.1
Jul	39.1	1.1	4	39.7	0.8	42.0	0.3	10	42.0	0.1	41.0	0.1	5	41.0	0.1
Aug	39.5	1.2	4	40.3	0.8	41.8	0.3	4	41.8	0.2	41.6	0.2	4	41.5	0.1
Sep	42.7	0.6	2	41.2	1.1	41.6	0.3	5	41.7	0.2	41.7	0.1	4	41.8	0.1
Oct				41.6		42.0	0.5	4	41.8	0.2	41.8	0.1	4	41.8	0.1
Nov	41.6	1.3	2	41.9	1.1	41.8	0.4	4	41.9	0.2	41.8	0.1	5	41.8	0.1
Dec	42.3	2.4	5	42.6	0.7	42.1	0.2	4	42.3	0.2	41.7	0.0	5	41.7	0.1
Annual	41.1	1.3	51	41.14	0.21	41.5	0.6	75	41.45	0.05	40.8	1.0	51	40.75	0.01
1984 Jan	43.6	1.6	5	43.4	0.6	43.2	0.3	5	43.0	0.2	41.6	0.4	4	41.6	0.1
Feb	43.6	2.5	2	43.7	1.0	43.4	0.4	4	43.5	0.3	41.6		1	41.6	0.2
Mar				43.7		44.2	0.7	3	43.7	0.3	41.4	0.3	5	41.4	0.1
Apr				43.6		43.7	1.1	3	43.5	0.3	41.3	0.0	4	41.4	0.1
May				43.6		42.4	0.4	3	42.9	0.3	41.4	0.2	4	41.5	0.1
Jun	42.8	0.7	2	43.7	1.0	42.6	0.3	5	42.6	0.2	41.8	0.2	5	41.8	0.1
Jul	44.6	1.3	9	44.2	0.5	42.9	0.3	4	42.9	0.3	42.1	0.3	4	42.0	0.1
Aug	44.4	1.4	9	44.4	0.5	43.6	0.3	4	43.4	0.3	42.5	0.1	4	42.6	0.1
Sep	43.8	1.2	6	44.1	0.6	43.7	0.4	5	43.6	0.2	43.0	0.2	5	43.0	0.1
Oct	43.8	1.5	4	43.8	0.7	43.4	0.4	4	43.5	0.3	43.0	0.1	4	43.0	0.1
Nov				43.6		43.3	0.4	3	43.5	0.3	42.9	0.3	5	43.0	0.1
Dec	43.3	1.9	4	43.3	0.7	44.0	0.6	4	44.1	0.3	42.8	0.2	11	42.9	0.1
Annual	43.7	0.6	41	43.75	0.21	43.4	0.5	47	43.35	0.07	42.1	0.7	56	42.13	0.03

Table 3—*continued*

	STM				
	Data	σ_d	N	Spline	σ_s
1981 Jan				43.7	
Feb				44.5	
Mar	45.6	0.7	4	45.3	0.5
Apr	45.6	0.6	7	45.6	0.4
May	46.0	0.7	6	46.2	0.4
Jun	44.8	2.3	9	44.6	0.3
Jul	37.5	1.6	8	37.3	0.3
Aug	32.7	1.0	10	33.0	0.3
Sep	36.0	1.8	7	35.5	0.4
Oct	39.3	2.2	8	39.5	0.3
Nov	43.2	1.4	9	42.9	0.3
Dec	43.3	1.0	2	44.1	0.7
Annual	41.6	4.5	72	41.82	0.11
1982 Jan	44.7	1.0	3	44.6	0.4
Feb	45.3	0.3	6	45.4	0.3
Mar	46.0	0.4	7	45.9	0.3
Apr	46.0	0.6	8	46.0	0.2
May	45.7	1.2	6	45.8	0.3
Jun	44.7	0.8	4	44.6	0.3
Jul	38.3	3.4	3	38.6	0.4
Aug	32.6	1.0	9	32.7	0.2
Sep	33.4	1.7	9	33.1	0.2
Oct	38.4	1.6	6	37.8	0.3
Nov	42.7	1.8	7	42.0	0.3
Dec	44.0	1.3	6	44.3	0.3
Annual	41.8	4.9	74	41.69	0.08
1983 Jan	45.0	0.8	9	44.8	0.3
Feb	44.6	1.3	4	45.1	0.4
Mar	46.3	1.0	5	46.4	0.4
Apr	47.1	0.6	5	47.0	0.4
May	46.1	0.9	10	46.2	0.3
Jun	44.5	1.7	7	44.4	0.3
Jul	38.7	1.9	9	38.8	0.3
Aug	33.8	1.2	8	33.9	0.3
Sep	35.1	2.0	8	35.2	0.3
Oct	41.3	1.3	6	40.1	0.3
Nov	44.1	1.3	8	43.9	0.3
Dec	45.8	0.7	6	46.1	0.3
Annual	42.7	4.5	85	42.62	0.09
1984 Jan	47.6	1.0	7	47.5	0.4
Feb	47.7	1.2	7	47.8	0.4
Mar	48.7	0.9	7	48.6	0.4
Apr	49.0	1.5	8	49.1	0.4
May	47.7	1.4	9	47.7	0.3
Jun	45.2	1.5	7	45.3	0.4
Jul	40.8	2.4	9	40.6	0.3
Aug	35.7	0.7	8	36.0	0.4
Sep	38.6	2.9	7	38.4	0.4
Oct	42.9	1.3	3	42.4	0.6
Nov	44.8	1.0	7	44.8	0.4
Dec	47.1	0.9	7	47.0	0.4
Annual	44.7	4.3	86	44.57	0.11

and represent randomly and normally distributed noise. It follows from this that the standard error associated with the mean CO_2 concentration for a given interval of time (month, season, year) is $\sigma_i = \mathrm{RSD}/(N(i))^{\frac{1}{2}}$, where $N(i)$ is the number of samples in the interval i. The monthly and annual means calculated using daily values from the curves and the standard errors calculated using the expression above are given in Table 3. The means and sample standard deviations (σ_d) calculated directly from the selected flask data are also given in Table 3. The mean values and uncertainties obtained from the best fit curves represent our best estimates of these parameters. Monthly and annual means calculated directly from the data are subject to incorrect weighting due to unevenly spaced data. The interpolating feature of the smoothing spline eliminates this problem. In addition, the uncertainties, σ_s, calculated from the curve fitting analysis are due only to the residual random noise. We emphasize that the σ_s are statistical uncertainties. They are not absolute uncertainties and do not take into account possible systematic errors or biases. Note that σ_d also includes the variation due to seasonality, so it is not a good measure of how well a mean value is determined.

While the residual standard deviation is a good measure of the scatter of the individual data points, the cubic spline curve itself is actually better determined than $\pm$RSD. To demonstrate this we took the best fit curve points at the actual sample dates and added noise having a random, normal distribution with $\mu = 0$ and $\sigma = \mathrm{RSD}$. We then fit a curve to these newly obtained points and calculated the root mean square (RMS) difference between the artificial curve and the original best fit to the data. The mean RMS difference, $\overline{D}$ (rms), calculated for each site from 10 artificial data sets is given in Table 2. This value is a measure of the uncertainty at any point of the best fit curve due to the scatter of the data. Examples of the curves generated with randomized noise are shown in Fig. 5. Since this empirically determined value can be thought of as the standard error of a point on the curve we can write

$$\overline{D}\ (\mathrm{rms}) = \mathrm{RSD}/(N_{\mathrm{eff}})^{\frac{1}{2}}, \qquad (2)$$

where N_{eff} is the effective number of data points used to determine a point on the curve. This equation has been solved for N_{eff} at each site

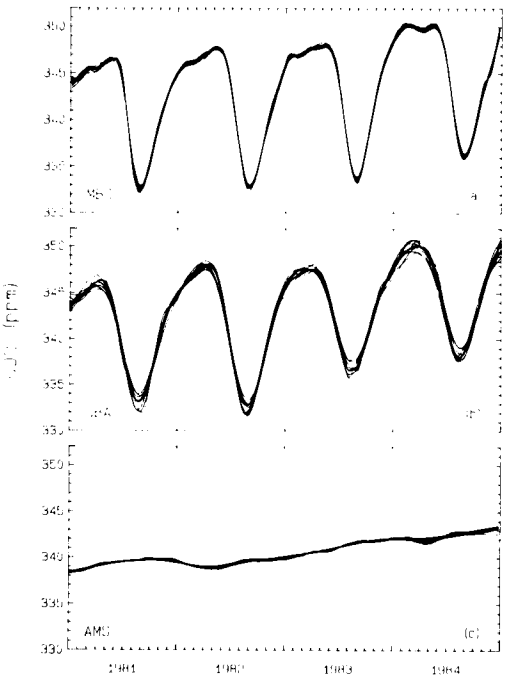

Fig. 5. Examples of the family of curves generated by applying random noise with mean = 0 and σ = RSD to the best fit curves to the data, and then fitting a curve to the artificial data. Each example shows ten artificial curves in addition to the original best-fit curve.

(Table 2). From N_{eff} and the average sampling frequency at each site, $\bar{f}$ (Table 2), the effective averaging time, or bandwidth, of the cubic spline fit, T_{eff}, is calculated. The averaging time thus calculated varies from 2 to 7 weeks with an average of about 1 month.

After we had performed the above described Monte Carlo calculations to determine the standard error of the curves, we found an expression for the filtering properties of the spline (Craven and Wahba, 1979). When the data are equally spaced, the spline is a low pass Butterworth filter with a transfer function proportional to

$$\frac{1}{1+\lambda\omega^4}, \tag{3}$$

where ω is the angular frequency, and λ is Craven and Wahba's stiffness parameter. The parameter λ is related to p by

$$\lambda = \frac{1}{N}\frac{1-p}{p}\{Dy(i)\}^2. \tag{4}$$

We can define the point at which the transfer function has fallen to 0.5 as the frequency cutoff of the filter and the inverse of that as the effective averaging time in the time domain (T'_{eff}). That gives us a definite relation between T'_{eff} and p. We have calculated T'_{eff} in this way for each curve from the given values of p (Table 2). T'_{eff} determined in this way is higher than what we found from the Monte Carlo calculations. The Monte Carlo simulations correspond more closely to a frequency cutoff point where the transfer function has fallen to 0.25. The comparison of these two different ways of estimating the bandwidth of the filter is crude: frequency cutoff points are not well defined and the data themselves are not equally spaced.

The summer drawdown of CO_2 at high northern latitudes possesses significant high frequency components and the splines don't pass these unattenuated. When the noise level is higher, the passband automatically adjusts to lower frequencies. An alternate approach would be to fix the passband, but then we would introduce spurious variability in a high noise record while leaving signal unresolved in a record with low noise.

Another manifestation of the frequency response of our filter showed up in the Monte Carlo calculations. If the original best fit curve underfits the summer drawdown and we inject random noise around the original curve to define artificial data sets, then the new curve fits to the artificial data will also underfit the drawdown because the high frequencies are again attenuated. We found that the original curve fit tended to lie at the lower edge of the family of artificial curves during the summer drawdown periods (Fig. 5). The effect of this limitation of the curve fitting method on determining the CO_2 seasonal cycle amplitude is discussed below.

4. Discussion

The following analyses of the global distribution and variation of atmospheric CO_2 concentration are based on the best fit cubic spline curves presented above. The curves are used to ensure that mean values are weighted appropriately when data are missing or unevenly spaced. This also allows the calculation of uncertainties, due to residual random noise, associated with the derived

parameters. The uncertainties calculated in this way are not absolute uncertainties and do not include the effects of possible systematic errors such as calibration or analytical biases. Since we are comparing data from samples collected by the same method and analyzed on the same apparatus, we believe that biases of this type, if they exist, are likely to be the same for all sites. These types of biases will not affect the analyses presented here.

Other sources of error which might affect these analyses are the effects of storage time, which varies among sampling sites, and variable amounts of water vapor in the samples. The flask data from SPO clearly show that relatively dry samples undergo no detectable change in concentration during storage. The last samples collected before station closing in February are analyzed within several weeks. The samples collected after station closing are analyzed nearly a year later and no discontinuity in the time series is observed. This result differs from Tanaka et al. (1983, 1987b) who find decreases in CO_2 concentration in dry samples of up to 1 ppm during one year. At other sites, the water vapor content of the samples is higher and more variable than at SPO. In moist air samples it is possible that increases in CO_2 occur over time (Komhyr et al., 1985a). Since most of our samples are analyzed within several weeks of collection, these effects probably contribute errors of less than 0.2–0.3 ppm. Errors introduced by storage and water vapor effects may or may not be included in the calculated statistical uncertainties, depending on whether they occur randomly or systematically. These types of errors may affect comparisons among sites.

Biases introduced during sample collection, such as always collecting samples on the same day of the week or at the same time of day, which happens not to be a representative day or time, could also affect comparisons among sites. To detect this type of bias would require information not available to us, so we mention the possibility, but will not pursue it further.

One possible source of a systematic error which could affect the internal consistency of the data is the change from "hand aspirated" to the portable battery powered pump method of collecting samples. This change was accompanied by an increase in the number of sample pairs meeting the 0.5 ppm criterion, but in general, a discontinuity in the CO_2 concentration record was not observed. An exception to this was found in the data from AMS. We have compared the GMCC CO_2 flask sample data to the data of the Centre des Faibles Radioactivites (CFR) collected by continuous in situ infrared analysis (Gaudry et al., 1983; Ascencio-Parvy et al., 1984). A comparison of annual and monthly means and individual flask values with hourly continuous analyzer values clearly shows that prior to the introduction of the portable pressurizing unit at AMS in March 1982, the GMCC data are higher than the CFR data by ~ 1 ppm. The GMCC data from March 1982 to the present agree extremely well with the CFR data (A. Gaudry, personal communication). Although we will report the AMS data with no actual adjustment, for the following analyses, we have adjusted the 1981 data by -1.0 ppm. It is possible that the PSA data for 1981 are also high since they were collected by the hand aspiration method and were stored for about the same length of time as the AMS samples. Since we have no independent record for comparison, no adjustment will be made. However, the 1981 PSA data should be viewed with some caution.

Since different curve-fitting methods were used, the monthly and annual means for 1981 and 1982 (Table 3) are somewhat different from those in Komhyr et al. (1985a). The results in Table 3 are internally consistent for the period 1981–84, thus bracketing the 1982–83 ENSO event. The following discussions are based on this analysis and comparisons of the overall features with the analysis of Komhyr et al. (1985a) are made where appropriate.

4.1. Latitudinal CO_2 distribution

To extract the variation of CO_2 concentration with latitude and time from the flask data, the best fit spline curves were digitized at two-week intervals and a matrix of the biweekly values versus latitude was constructed. From this matrix a surface with grid points spaced at two week by 10° latitude intervals was calculated using routines from the DISSPLA graphics package (ISSCO, 1981). Data for NWR, MLO, AZR, and KEY were not included in the matrix to avoid complications due to continental influences (NWR, KEY, AZR) and vertical gradients (NWR, MLO). Since the remaining sites are included regardless of longitude, the result is a

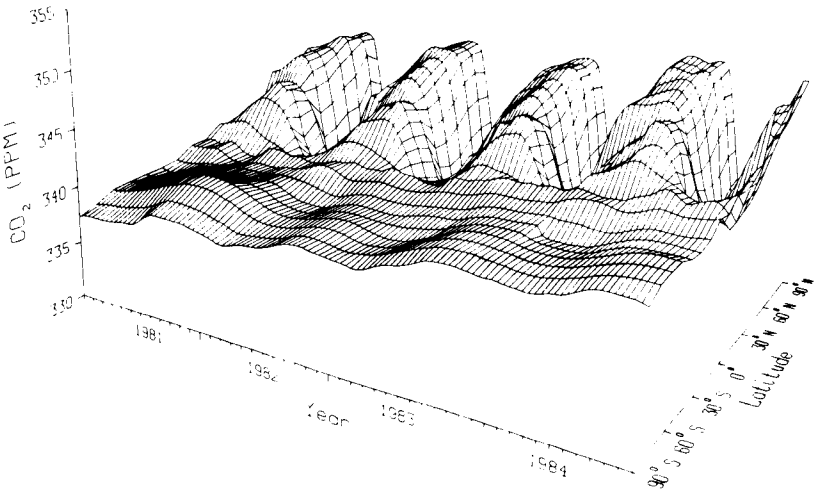

Fig. 6. Three-dimensional representation of the variation of CO_2 concentration with latitude and time determined from the flask network data.

smoothed, "zonally averaged" representation of CO_2 variation in the remote marine boundary layer (Fig. 6). The zonality implicit in this representation will be discussed below.

The highly smoothed surface obtained in this way extends the earlier result of Komhyr et al. (1985a) and summarizes many major features of the CO_2 distribution. The difference in both the amplitude and phase of the seasonal cycles in the northern and southern hemispheres is clearly shown. The reversal of the north–south CO_2 gradient during the northern hemisphere summer is also well depicted, graphically illustrating that the CO_2 fluxes between the atmosphere and the biosphere are larger than the approximately 5 Gt of fossil fuel carbon released to the atmosphere each year. The seasonality of the atmospheric CO_2 concentration is mainly the result of the seasonal imbalance between photosynthesis and respiration of land plants. The relatively small latitudinal and seasonal variation observed in the southern hemisphere illustrates that CO_2 sources and sinks are smaller there than in the northern hemisphere. In fact, the variations are so small it is difficult to determine the relative contributions from northern and southern hemisphere biospheric, marine, and anthropogenic fluxes (see, for example, Pearman and Hyson, 1986).

The annual mean CO_2 concentrations for the flask network sites (Table 3) are plotted versus sin(latitude) in Fig. 7. The plots for 1981 and 1982

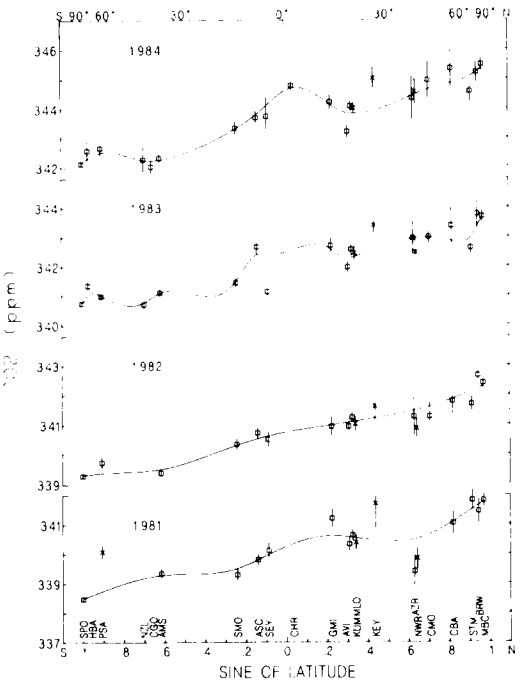

Fig. 7. Annual mean CO_2 concentrations versus sin(latitude) for the GMCC flask network sites, 1981–84. The smooth curves are cubic spline fits to the points represented by squares. The crosses were not used in the curve fits (see text). The vertical bars represent $\pm 3^*\sigma_s$, where σ_s is the statistical uncertainty of the annual mean (Table 3).

are similar to plots in Komhyr et al. (1985a). The main difference is that the curves in Fig. 7 are cubic spline curves fitted to the data providing a somewhat more objective basis for discussing the CO_2 latitude gradient and its interannual variability than the hand-drawn curves previously used. The curves were determined using the method of Reinsch (1967) with the smoothing parameter, S, set equal to N, the number of points. In this case the stiffness of the spline is determined by the weighting parameter $Dy(i)$ which represents the uncertainty associated with the ith point. To obtain the curves in Fig. 7 we used

$$Dy(i) = 3^*\sigma_s(i), \tag{5}$$

where the $\sigma_s(i)$ are the statistical uncertainties of the annual means given in Table 3. The multiplicative factor 3 was chosen somewhat subjectively in that the curves thus obtained were judged by eye to be reasonably smooth but flexible enough to pick up major features in the global CO_2 gradient. While the weighting factors ($3^*\sigma_s$) overstate the uncertainty of the annual means, the fact that a smooth curve is obtained suggests that the longitudinal variability, which has heretofore been neglected in this discussion, is of the order of $3^*\sigma_s$. Thus the scatter of the points about the curves may be due to the fact that the atmosphere is not zonally well mixed and the CO_2 concentration at specific sites is affected by the location of regional sources and sinks as well as by atmospheric transport. The general representativeness of the zonal means, to within 0.5–1.0 ppm, has been supported by the results of flask samples collected aboard ships in remote ocean regions (Nickerson, 1986; Harris and Nickerson, 1984). As mentioned above, it is also possible that biases resulting from storage and water vapor effects may contribute a few tenths ppm to the scatter of the annual means.

Note that in Fig. 7 the means for NWR, KEY, and MLO are plotted but have not been used in fitting the curves to avoid continental (NWR, KEY) and vertical gradient (NWR, MLO) effects. SPO is included even though it is a high altitude site. The AMS annual mean for 1981 has been adjusted to agree with the CFR data and PSA was not used in obtaining the 1981 curve. The vertical lines in Fig. 7 represent $\pm 3^*\sigma_s$.

The north pole to south pole concentration difference determined from the GMCC flask network varies from 2.9 ppm in 1983 to 3.4 ppm in 1981, with a mean of 3.1 ppm ($\sigma = 0.2$ ppm). There is no evidence for a trend in this difference over the four years studied. The mean difference is less than the 4–5 ppm reported by Pearman et al. (1983) based on an analysis of provisional data, but is not significantly different from that reported by Komhyr et al. (1985a) and Pearman and Hyson (1986). The mean north–south difference is generally believed to be maintained by the emissions of fossil fuel CO_2, primarily in midlatitudes of the northern hemisphere.

The second most prominent feature of the mean latitude gradients is the local maximum in CO_2 concentration occurring at, or slightly north of, the equator. Previous studies have shown that this enhancement of ~ 1 ppm in atmospheric CO_2 results from a source of CO_2 in the equatorial oceans (Mook et al., 1983; Pearman et al., 1983; Pearman and Hyson, 1986). In the equatorial Pacific, the source is in an area of surface water highly ($\sim 30\%$) supersaturated with CO_2. The supersaturation is due to the upwelling of relatively cold, nutrient-rich water containing more dissolved CO_2 than the warmer surface waters (Keeling and Revelle, 1985; Feely et al., 1987). Part of this excess CO_2 is released to the atmosphere as this water warms and is advected westward in the South Equatorial current.

The mean latitude gradients for the four years 1981–84 suggest the occurrence of, and recovery from, an apparent anomaly in the equatorial CO_2 source. The equatorial maximum evident in the meridional gradients prior to 1982 (Komhyr et al., 1985a) is largely absent in 1982. A partial recovery of the equatorial feature occurs in 1983 but it appears flatter and farther south than normal. By 1984, the equatorial atmospheric CO_2 enhancement appears to have returned to its normal magnitude (~ 1 ppm) and location. The equatorial CO_2 feature was less well determined in 1981 through 1983 due to the lack of a truly equatorial sampling location, but it has been shown elsewhere to be a persistent feature of the meridional CO_2 distribution (Keeling and Heimann, 1986; Tanaka et al., 1987a). The addition of CHR to the sampling network in 1984, in cooperation with C. D. Keeling of the Scripps Institution of Oceanography (SIO), has resulted in

a much better determination of the equatorial feature since 1984.

The absence of this feature from the 1982 latitude gradient has been attributed to a decrease in the equatorial CO_2 marine source during the 1982–83 El Niño/Southern Oscillation (ENSO) event (Komhyr et al., 1985a; Feely et al., 1987). There is evidence that the weakening of the normal upwelling of cold nutrient rich water in the eastern equatorial Pacific, a characteristic of ENSO events, also lowers the relative supersaturation of CO_2 in the surface ocean water. Feely et al. (1987) and Keeling and Revelle (1985), have proposed that the combination of low pCO_2 relative to the atmosphere and lower wind speeds due to weakened trade winds may result in a significant decrease in the strength of the equatorial CO_2 source. However, while Thompson et al. (1986) are not able to rule out reduced upwelling and changes in wind stress as factors affecting the atmospheric observations, they suggest that variations in biospheric fluxes should also be considered. In any case, since fossil fuel emissions continued at a nearly constant rate of 5 Gt yr^{-1} during 1981–84 (Rotty, 1987), the absence of an equatorial marine CO_2 source of this magnitude would be expected to cause a decrease in the atmospheric CO_2 growth rate. This point will be discussed further in the section on growth rates.

In the latitude gradients (Fig. 7) there is also the suggestion of a local maximum occurring between the South Pole and 40°S. In 1981 the PSA data are questionable and have not been used in fitting the curve, so the pattern in the southern hemisphere is not very well determined. In 1982 the fitted curve is fairly flat in this region but note that the annual mean for PSA is higher than either SPO or AMS. The feature is determined better in 1983 and 1984 due to the addition of HBA to the network. Further, the data from NZL in 1983 and 1984 (even though NZL was not a representative site for this latitude and required heavy selection) and CGO in 1984, provide, with AMS, a tight constraint on the midlatitude portion of the curve. The 1983 and 1984 means for PSA and HBA indicate the possibility of a CO_2 source in this region. Whether this source is marine or related to atmospheric transport has not been determined. Care must be used in comparing SPO to PSA and HBA since the air arriving at high altitude in mid-continent may be of different origin and history than that arriving at the sea level sites along the Antarctic coast.

In examining these plots (Fig. 7) it is clear that determination of the latitude gradient depends on having suitable sampling sites at approximately 10° latitude intervals and that sites at certain latitudes are critical in defining the fine structure of the gradient. Fraser et al. (1983) have pointed out that resolving latitude gradients to a few tenths of a ppm per 10° of latitude is necessary to detect regional fluxes of $\sim$0.5 Gt yr^{-1}. To improve on the results shown here, in 1985 we began sampling at Alert, N.W.T., Canada (83°N, 62°W); Shemya Island, Alaska (53°N, 174°E); Midway Island (28°N, 177°W); and South Georgia Island (54°S, 38°W). These sites are intended either to fill gaps in the latitude coverage (Alert, South Georgia Island) or to replace an existing site with one more regionally representative for a zone (Shemya Island and Midway Island as opposed to Cold Bay and Key Biscayne). Sampling at Cape Grim, Tasmania (CGO) in cooperation with G. Pearman and P. Fraser of the Commonwealth Scientific and Industrial Research Organization began in 1984 and sampling at NZL was discontinued in 1985 after it was established that CGO was a more suitable site for representative measurements at this latitude. We have yet to find a suitable site to fill the largest gap remaining, the 24° between SMO and AMS.

4.2. Seasonal variations

To examine the seasonal cycle of the data series it is necessary to remove the long-term increase due to fossil fuel combustion. Previous studies have removed this trend by approximating it with an exponential function (Bacastow et al., 1985) or by fitting a cubic spline with knots every 12 months and then subtracting the trend from the record (Komhyr et al., 1985a). Recent information on fossil fuel emissions indicates that the use of an exponential function for the long-term trend is no longer appropriate (Rotty, 1987). Due to problems associated with fixed node cubic splines this method is no longer recommended for CO_2 data analyses (Enting, 1986).

In this work we have determined the long-term trend by calculating a 12-month running mean which effectively removes signals with periods

of one year and all of its higher harmonics. The 12-month running mean was applied to the best fit curve values at biweekly intervals, as we have found that the biweekly values are sufficient to describe the best fit curves. Since the first and last six months of record are lost in calculating a 12-month running mean, we have used the last six months of 1980 and the first six months of preliminary 1985 data to obtain four complete years of running mean. The running mean values determined at biweekly intervals were then fit with the cubic spline described above and this curve was subtracted at daily intervals from the best fit curve to the data to obtain the detrended CO_2 record.

The statistical uncertainty of the detrended record is dominated by $\overline{D}$ (rms), the standard deviation of the best fit curve. The standard deviation of the 12-month running mean (σ_{RM}) is much smaller. Values for $\overline{D}$ (rms) and σ_{RM}, are given in Table 2.

The amplitude of the seasonal cycle in the detrended record will be discussed using the notation of Komhyr et al. (1985a) where the peak-to-peak amplitude for a year is given by

$$CPP = CP^+ + CP^-. \quad (6)$$

CP^+ is the CO_2 maximum above the long-term trend and CP^- is the magnitude of the minimum below the trend. The statistical uncertainty of the amplitude is then

$$(2)^{\frac{1}{2}} * \overline{D} \text{ (rms)}. \quad (7)$$

The seasonal cycle characteristics for 1981–84 are given in Table 4. For the four years of data, the average of the peak-to-peak amplitude and the sample standard deviation for each site are also tabulated. Since the records for CMO, HBA, CHR, and CGO are too short to calculate a satisfactory 12-month running mean, the seasonal amplitude characteristics have been calculated using the best fit curve and an estimate of the growth rate.

Since changes in the seasonal cycle of CO_2 concentration are likely to result primarily from changes in the activity of the terrestrial biota

Table 4. *Amplitude of the seasonal cycle*

	1981			1982			1983			1984				
Site	CP^+	CP^-	CPP	CP^+	CP^-	CPP	CP^+	CP^-	CPP	CP^+	CP^-	CPP	$\overline{CPP}$	σ
AMS	0.45	0.41	0.86 (0.18)	0.37	0.62	0.99 (0.18)	0.28	0.24	0.52 (0.18)	0.39	0.59	0.98 (0.18)	0.84	0.22
ASC	1.07	0.76	1.83 (0.34)	0.76	1.00	1.76 (0.34)	0.77	0.98	1.75 (0.34)	1.44	1.21	2.65 (0.34)	2.00	0.44
AVI	3.69	4.81	8.50 (0.40)	3.32	5.08	8.40 (0.40)	3.57	3.83	7.40 (0.40)	5.05	5.55	10.60 (0.40)	8.73	1.35
AZR	4.47	5.43	9.90 (0.87)	5.71	7.65	13.36 (0.87)	3.28	5.06	8.34 (0.87)	3.61	5.37	8.98 (0.87)	10.15	2.24
BRW	5.83	10.83	16.66 (0.81)	5.20	10.42	15.62 (0.81)	4.88	10.82	15.70 (0.81)	5.07	9.55	14.62 (0.81)	15.65	0.83
CBA	5.49	9.09	14.58 (0.85)	6.30	10.22	16.52 (0.85)	4.76	8.24	13.00 (0.85)	5.01	7.96	12.97 (0.85)	14.27	1.68
CGO												1.29 (0.31)		
CHR												3.84 (0.40)		
CMO						10.46 (1.09)			9.87 (1.09)			9.09 (1.09)	9.81	0.69
GMI	2.80	3.17	5.97 (0.46)	2.94	4.20	7.14 (0.46)	3.40	3.42	6.82 (0.46)	2.84	3.06	5.90 (0.46)	6.46	0.62
HBA									1.65 (0.30)			0.84 (0.30)	1.25	0.60
KEY	3.04	3.86	6.90 (0.88)	3.45	4.37	7.82 (0.88)	3.11	3.75	6.86 (0.88)	3.22	4.30	7.52 (0.88)	7.28	0.47
KUM	4.12	4.34	8.46 (0.39)	4.08	5.05	9.13 (0.39)	3.92	5.04	8.96 (0.39)	4.11	4.82	8.93 (0.39)	8.87	0.29
MBC	4.81	9.98	14.79 (0.47)	5.16	9.89	15.05 (0.47)	4.98	10.92	15.90 (0.47)	5.22	9.64	14.86 (0.47)	15.15	0.51
MLO	3.21	3.40	6.61 (0.34)	3.04	3.82	6.86 (0.34)	3.50	3.38	6.88 (0.34)	3.11	3.22	6.33 (0.34)	6.67	0.26
NWR	4.01	5.48	9.49 (0.70)	4.66	6.13	10.79 (0.70)	4.16	6.76	10.92 (0.70)	4.26	6.48	10.74 (0.70)	10.49	0.67
PSA	0.70	0.53	1.23 (0.22)	0.48	0.68	1.16 (0.22)	0.63	0.72	1.35 (0.22)	0.91	0.55	1.46 (0.22)	1.30	0.13
SEY	2.04	1.30	3.34 (0.63)	1.78	0.74	2.52 (0.63)	1.73	1.63	3.36 (0.63)	0.83	1.34	2.17 (0.63)	2.85	0.60
SMO	0.76	0.53	1.29 (0.31)	1.05	0.60	1.65 (0.31)	0.56	0.54	1.10 (0.31)	0.89	0.65	1.54 (0.31)	1.40	0.25
SPO	0.71	0.40	1.11 (0.12)	0.63	0.71	1.34 (0.12)	0.61	0.76	1.37 (0.12)	0.62	0.56	1.18 (0.12)	1.25	0.13
STM				4.34	9.97	14.31 (0.60)	4.88	9.85	14.73 (0.60)	5.07	9.18	14.25 (0.60)	14.43	0.26

The values in parentheses are the statistical uncertainties of the peak-to-peak amplitudes as described in the text. σ denotes the sample standard deviation of CPP for the available years.

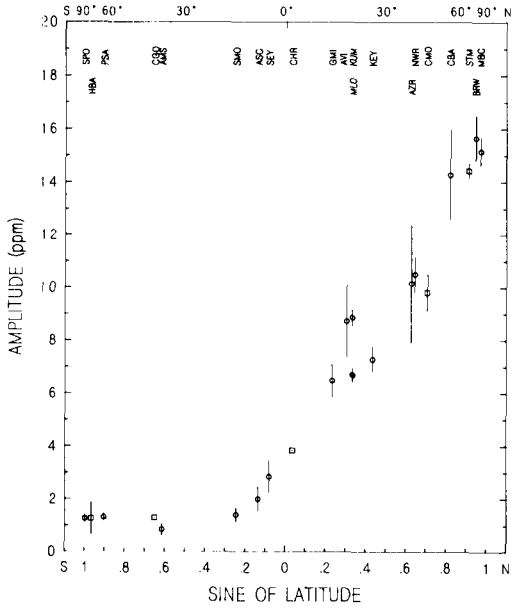

Fig. 8. The latitude dependence of the mean peak-to-peak amplitude at the flask network sites. Circles indicate 4-year means while squares indicate means for less than four years. The error bars are the sample standard deviations (Table 4). The circle for MLO is filled to distinguish it from KUM.

(Bacastow et al., 1985) we examined the seasonal cycle characteristics of the flask network data for evidence of significant changes. Due to the large interannual variability of these parameters (Table 4), no significant trends in CP^+, CP^-, or CPP were observed. Further, there was no tendency for the variability in these parameters to be correlated or even similar among the sites. While studies of longer records (e.g., Bacastow et al., 1985; Enting, 1987) find evidence for an increase in the amplitude of the northern hemisphere seasonal cycle during the past decade, it is clear that the year-to-year variability is too large for such changes to be observed in a 4-year record.

The latitude dependence of the mean peak-to-peak amplitude is shown in Fig. 8. The error bars are the sample standard deviations (σ in Table 4) except for CGO and CHR for which we have only one value. The maximum amplitude is ~ 16 ppm at BRW and the amplitude may drop off further north. The seasonal amplitude decreases smoothly through the northern hemisphere to ~ 1 ppm at SMO. Throughout the southern hemisphere the seasonal amplitude changes very little with latitude. These results are consistent with those of Komhyr et al. (1985a) and Pearman and Hyson (1986), although, by including the statistical uncertainty, we find no evidence for significant variation of the seasonal amplitude at the surface from SMO to SPO.

It should be pointed out that the determination of the seasonal amplitude depends very much on the behavior of the cubic spline fit. Examination of Fig. 2 indicates that there is a tendency to underfit the minimum of the seasonal cycle especially at high latitude northern hemisphere sites such as BRW and CBA. In these cases the measured values in the minimum of the trough tend to lie below the best fit curves. Similar effects have been observed using other curve fitting procedures (Keeling et al., 1985). Several factors contribute to this problem. The high frequency nature of the minimum tends to be filtered out by curves which are intended to smooth the high frequency noise in other parts of the record. The relatively low sampling frequency results in little weight being given to this portion of the record relative to the overall fit to the 4-year record. Finally the high natural variability which is often observed at this time of year further reduces the effect of these points. The result is that the high northern latitude seasonal amplitudes may be underestimated by as much as 1–2 ppm. While some of this error contributes to the interannual variability, and thus to the error bars in Fig. 8, it is likely that underfitting is a systematic effect which is not accounted for by the statistical uncertainty.

Possible solutions to this problem are more frequent sampling during the summer and selection of sampling sites where the variability during summer is low. These effects can be seen graphically by comparing CBA and MBC in Fig. 2. At MBC samples are collected twice per week and the variability is small even during summer. This results in a good fit at the summer minimum. At CBA samples are also collected twice per week, but data selection due to occurrence of non-background conditions reduces the number of reliable samples. This, in addition to the larger variability especially in summer, results in underfitting at the summer minimum. In order to determine trends in the amplitude of the annual

e 5. *Phase of the seasonal cycle*

1981		1982		1983		1984				
DD	BU	DD	BU	DD	BU	DD	BU	$\overline{DD}$	σ	$\overline{BU}$
01 Jan (8)	09 Apr (12)	29 Jan (8)	12 Jul (11)	27 Oct (16)	24 Jun (17)	05 Mar (8)	27 Jun (7)	07 Jan	55	10 Jun
29 Jan (12)	10 Jul (5)	21 Nov (7)	11 Apr (7)	18 Oct (15)	11 Apr (16)	15 Jan (11)	01 Jun (14)	13 Dec	48	16 May
21 Jul (3)	27 Dec (3)	15 Jul (2)	12 Dec (4)	19 Jul (2)	13 Jan (5)	16 Jul (2)	22 Dec (3)	18 Jul	3	26 Dec
25 Jun (5)	14 Dec (9)	17 Jun (4)	05 Nov (5)	22 Jun (8)	29 Nov (10)	22 Jun (5)	02 Dec (6)	22 Jun	3	28 Nov
25 Jun (2)	13 Nov (6)	29 Jun (3)	18 Nov (6)	30 Jun (2)	10 Nov (5)	27 Jun (2)	27 Nov (6)	28 Jun	2	17 Nov
17 Jun (3)	13 Nov (6)	20 Jun (3)	15 Nov (4)	12 Jun (4)	06 Nov (7)	10 Jun (3)	04 Nov (6)	15 Jun	5	10 Nov
24 Jul (4)	25 Jan (5)	24 Jul (4)	11 Jan (8)	04 Aug (4)	25 Jan (9)	07 Aug (5)	28 Jan (11)	30 Jul	7	22 Jan
15 Jul (9)	26 Dec (12)	04 Jul (8)	26 Dec (11)	15 Jul (8)	29 Dec (9)	07 Jul (8)	14 Dec (44)	10 Jul	6	24 Dec
07 Jul (2)	04 Jan (4)	11 Jul (4)	01 Jan (7)	10 Jul (2)	17 Jan (7)	14 Jul (2)	18 Dec (9)	11 Jul	3	02 Jan
08 Jul (1)	27 Nov (5)	05 Jul (1)	02 Dec (5)	03 Jul (1)	12 Nov (3)	04 Jul (1)	04 Dec (2)	05 Jul	2	26 Nov
14 Jul (4)	10 Jan (5)	22 Jul (3)	11 Jan (7)	26 Jul (3)	13 Jan (9)	24 Jul (3)	10 Jan (8)	22 Jul	5	11 Jan
14 Jun (4)	13 Nov (7)	13 Jun (3)	06 Dec (18)	16 Jun (4)	15 Nov (4)	21 Jun (3)	12 Nov (10)	16 Jun	4	19 Nov
	09 May (20)	17 Jan (13)	27 Jul (14)	13 Dec (13)	16 Jun (14)	01 Jan (13)	20 Jul (13)	01 Jan	18	25 Jun
08 May (12)	05 Dec (23)	11 May (18)	12 Jan (25)	11 May (14)	27 Nov (38)	02 May (67)		08 May	4	15 Dec
27 Apr (9)	23 Dec (15)	21 Apr (7)	09 Aug (42)	21 Aug (14)	26 Dec (8)	05 May (8)	19 Aug (21)	27 May	58	19 Oct
	10 Jul (3)	05 Jan (10)	16 Jul (7)	03 Dec (10)	30 Jun (12)	04 Jan (19)	27 Jul (5)	25 Dec	19	13 Jul
			14 Nov (3)	28 Jun (2)	11 Nov (4)	25 Jun (3)	19 Nov (6)	27 Jun	2	15 Nov

he values in parentheses are the statistical uncertainties of DD and BU, in days, as described in the text. $\overline{DD}$ and $\overline{BU}$ are the mean drawdown
up dates and the σ are the sample standard deviations (days) for the available years.

cycle from flask data, long records (10 or more years) and frequent sampling (minimum of twice per week) would probably be needed to overcome the effects of statistical uncertainties and possible systematic errors in determining the amplitude of the cycle. We are also trying to develop a better algorithm to extract a smooth signal from the data that does not underestimate the summer minimum.

The phase of the seasonality in CO_2 concentration was examined using the detrended best fit curves. Because the dates when CO_2 reaches the maximum and minimum concentrations in the seasonal cycle are not very well determined due to the flatness of the slope combined with local and regional variability and the considerations of curve fitting mentioned above, the days when decreasing and increasing concentrations cross the 12-month running mean are used as indicators of the phasing of CO_2 drawdown (DD) and buildup (BU), respectively. These crossing dates vary less from year to year than the dates of minimum and maximum CO_2 and thus, are useful for examining the variation of the phase of the seasonal cycle with latitude and time (Komhyr et al., 1985a). The statistical uncertainties associated with DD and BU were determined by dividing the standard deviation of the best fit curve, $\overline{D}$ (rms), by the slope of the curve at DD and BU. The seasonal cycle phase characteristics are summarized in Table 5. As with the amplitude, DD and BU were examined for significant trends or patterns in the 4-year record but none were observed. The mean and standard deviation of DD and BU were calculated for each site, and are plotted versus latitude in Fig. 9.

In the northern hemisphere the drawdown (DD) occurs on the same day, within ± 1 week, each year at a given site. This suggests that the drawdown is closely related to a growing-season factor, such as increasing sunlight, which varies little from year to year. The drawdown occurs earliest at $\sim 50°$N in mid June, and occurs later both to the north and south (mid July at MBC and late July at GMI). This result must be due to the combined effect of at least three factors: the onset of photosynthesis, the temperature dependence of ecosystem respiration, and atmospheric transport.

At higher northern latitudes the growing season and therefore the CO_2 drawdown, starts later than farther south. Also any transport of the midlatitude seasonal signal to the north would result in a lag in the phase of the transported signal, depending on the transport time. Thus to the north, the local seasonality and transport both contribute to the phase lag of the CO_2 seasonality

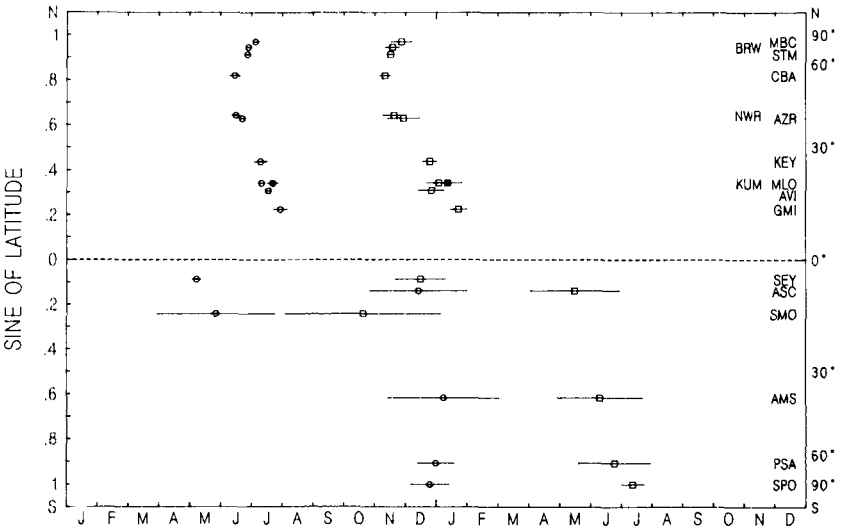

Fig. 9. The latitude dependence of the mean phase of the CO_2 seasonal cycle 1981–84. Circles represent the drawdown dates (DD) and squares represent the buildup dates (BU). The error bars represent the sample standard deviation (Table 5). The symbols for MLO are filled in to distinguish them from KUM.

with respect to 50° N. Southward of 50° N the situation is more complicated. Here the growing season starts earlier and in the tropics there is little or no seasonality in growth. In these latitudes, respiration is stronger and probably more closely matched in time with photosynthesis, resulting in a smaller local seasonal CO_2 amplitude. Therefore, the observed phase lag compared to 50° N must be due primarily to transport. It follows that also the amplitude of the seasonal cycle observed south of 50° N is due to transport from the north. The locally produced CO_2 seasonality must be so small that it is essentially masked by the signal transported from midlatitudes.

A similar pattern is observed in the CO_2 buildup in the northern hemisphere, although the date of the buildup is not as consistent at each site as it is for the drawdown. This suggests that the return of CO_2 to the atmosphere depends more strongly on more variable parameters such as temperature and moisture, rather than just length of day. Still, a well defined pattern is observed with the buildup first occurring at ~50° N during the second week of November. The buildup occurs later to both the north and south of 50° N, coming in late November at MBC and mid to late January at GMI. As in the case of the CO_2 drawdown, the latitudinal variation in the phase of the CO_2 buildup is due to a combination of transport and factors controlling the local seasonality. It is interesting to note that the drawdown and buildup at the high altitude MLO site tend to occur later than at KUM, again suggesting a phase lag due to (vertical) transport. This is confirmed by the seasonal amplitude at MLO which is 25% lower than at KUM.

These results, which are consistent with the analysis of Komhyr et al. (1985a), demonstrate that the variation of the phase of the CO_2 seasonality with latitude in the northern hemisphere is well determined from the flask network data. The interannual variability and the statistical uncertainty in determining the phase of the seasonality are comparable and relatively small. This latitudinal variation in seasonality can provide a powerful test for carbon cycle models since it results from the combination of local seasonality in the biospheric CO_2 fluxes and the transport of these signals through the northern hemisphere.

In the southern hemisphere, the variation of seasonality with latitude is not well defined (Fig. 9). At SMO and SEY the observed seasonality is not due to changes in local biospheric fluxes but is the result of seasonal variations in the transport of northern air across the intertropical convergence zone (ITCZ) into the southern hemisphere. The transport of northern hemisphere air to SMO has been observed previously to occur seasonally but is subject to considerable variability (Bortniak, 1981; B. Halter and J. Harris, personal communication). The situation at SEY is similar and the effect of intrusions of northern hemisphere air on CH_4 concentrations supports this interpretation of the observed CO_2 seasonality (Steele et al., 1987).

The seasonality at ASC, which is between SMO and SEY in latitude, does not appear to be affected by transport of northern air, suggesting that interhemispheric transport in the Atlantic is different from that in the Pacific and Indian Oceans. At ASC, AMS, PSA, and SPO the drawdown occurs in December–January and the buildup in May–June. Although there is considerable variability in these dates, the southern hemisphere seasonality is, in general, 6 months out of phase with the northern hemisphere. In the southern hemisphere we find no evidence for the propagation of a seasonal signal from midlatitudes to higher and lower latitudes. This reflects the absence in the southern hemisphere of the strong forcing by the terrestrial biosphere which drives the northern hemisphere CO_2 seasonality.

The seasonality in the southern hemisphere is difficult to determine because it is small relative to the uncertainties in the data. These uncertainties are the result of both natural variability and problems of data frequency, quality, and analysis. Therefore, the southern hemisphere is less of a constraint on carbon cycle models. We are not able to determine from these data whether the dominant source of the observed seasonality is interhemispheric transport, the terrestrial biosphere, or local sea/air exchange. As suggested by Pearman and Hyson (1986), measurements of carbon isotopes are needed to resolve this issue.

4.3. CO_2 growth rates

The long-term increase in atmospheric CO_2 due to fossil fuel combustion can be well determined by measurements at a small number of carefully chosen sites, for example MLO and SPO. Variations in the growth rates observed at these

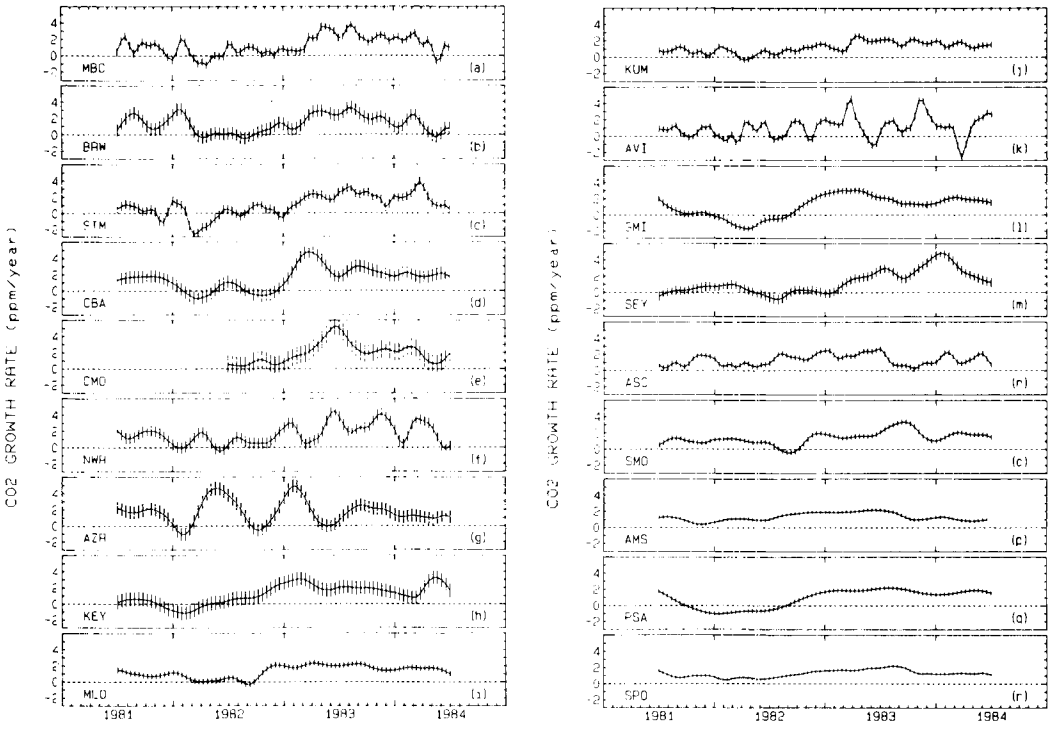

Fig. 10. The time dependence of the CO_2 growth rate at 18 flask network sites. The error bars indicate the statistical uncertainty of the growth rate curves, $(2)^{\frac{1}{2}}\overline{D}$ (rms) (see text and Table 2).

sites have been shown to be related to changes in fossil fuel use and natural variations in the global carbon cycle (Bacastow et al., 1980; Gammon et al., 1985). The flask sampling network provides the opportunity to examine the spatial as well as the temporal variability of the growth rate. The spatial variability of the growth rate may provide insight to the variability of regional, as opposed to global, CO_2 sources and sinks.

The CO_2 growth rates for the flask network sites were calculated using the biweekly values of the best fit curves. Differences between corresponding biweekly values in consecutive years were computed, and these defined the growth rate values (ppm yr^{-1}) assigned to the midpoints. This method is equivalent to taking the derivative of a one-year running mean using values at biweekly intervals. The statistical uncertainty (one standard deviation) of the growth rate is then $(2)^{\frac{1}{2}} * \overline{D}$ (rms), where $\overline{D}$ (rms) is the statistical uncertainty of the best fit curve. The growth rates for each site are plotted in Fig. 10. An important feature in this figure is the inclusion of a measure of the statistical uncertainty of the calculated growth rates. While Bacastow (1976) acknowledged the problem involved in judging the significance of growth rates determined by differentiating smooth curves fit to noisy data, most subsequent analyses have failed to address this point (e.g., Keeling et al., 1985; Komhyr et al., 1985a; Thompson et al., 1986).

Fig. 10 clearly shows that the uncertainty in determining the time variation of the growth rate is relatively large and varies considerably among the sites. The error bars in Fig. 10 result from the scatter of the measured points about the best fit curve. Thus the uncertainty tends to be higher in the northern hemisphere where the natural variability in the atmosphere is greater due to the proximity of sources and sinks (Fig. 2). Interpreting the growth rate plots is further complicated by the fact that even at sites with similar statistical uncertainties (e.g., MLO and KUM) the high frequency structure of the derivatives can be very different. Since the smoothness of the growth rate

curves depends on the smoothness of the best fit curves, this illustrates how small differences in the smoothness of the best fit curves are amplified when growth rates are determined. Taken together, the relative magnitudes of the statistical uncertainty (error bars in Fig. 10) and the high frequency structure of the growth rates indicate that a longer smoothing time is appropriate for analyzing the growth rates than for the data per se, so that short-term growth rate variations of no statistical significance would be filtered out. A longer smoothing time would also reduce the effect of small changes in the phase of the seasonal cycle, which appear in Fig. 10 as large swings in the growth rate.

Of the 18 growth rate records shown in Fig. 10, 16 show a similar pattern: a growth rate minimum in 1982 followed by a maximum in 1983. The maxima and minima are clearly significant. Considerable variability in the timing and magnitude of the minima and maxima among the sites is apparent. The two exceptions to the pattern are AZR and AVI which are dominated by large oscillations in growth rate throughout the records. Examination of Fig. 10 shows that the largest oscillations at both AZR and AVI are peaks and troughs separated by one year intervals, a pattern which could be caused by variations in the phase of the seasonal cycle. Fig. 8 and Table 4 show that the variability in the seasonal cycles at both AZR and AVI is large enough to account for the growth rate oscillations. This is due to problems of data quality, selection, and curve fitting as mentioned above.

A number of previous studies have found a correlation between the Southern Oscillation Index (SOI) and the CO_2 growth rate (e.g., Bacastow, 1976, 1977; Bacastow et al., 1980; Komhyr et al., 1985a), and a similar relationship has been observed in the growth rates presented here. To quantify this observation we have calculated the cross-correlation coefficients of the growth rates of Fig. 10 with the SOI (Climate Analysis Center, 1986). Based on the studies cited above, we compute correlations only where the SOI leads the growth rate records. Caution should be used in interpreting the correlations between short records, especially if only one event occurs during the record.

Significant negative correlations were found at 16 of the 18 sites considered. The maximum cross-correlation coefficients and the lag in months when the maximum correlation occurs are given in Table 6. The significance of the correlation coefficient is judged by comparing it to the standard deviation of the correlation coefficient near zero lag if the two series are uncorrelated, Table 6 (Box and Jenkins, 1976). The lags ranged from 2 months at ASC to 12 months at SEY and there is a tendency for the lags to be shorter near the equator and longer toward the poles. No significant correlation is found for AVI and AZR due to the high variability of the growth rates mentioned above.

The global CO_2 growth rate has been determined using the latitudinally weighted global average CO_2 concentration calculated from the flask network data. The result in Fig. 11 is similar to a figure published previously based on a preliminary analysis of these data (Harris and Nickerson, 1984). The SOI is also shown for comparison. The maximum correlation between the global growth rate and the SOI is -0.70 with a lag of 7 months, and a standard deviation near 0 lag (if there is no correlation) of 0.38. While the maximum correlation occurs at 7 months there is actually a rather broad (± 2 months) region of high correlation.

Table 6. *Correlation of CO_2 growth rate and SOI*

Site	r_{max}	σ*	Lag (months)
AMS	−0.87	0.37	5
ASC	−0.67	0.28	2
AVI	−0.25	0.19	7
AZR	−0.26	0.21	1
BRW	−0.81	0.31	8
CBA	−0.68	0.32	8
GMI	−0.65	0.40	4
KEY	−0.58	0.37	5
KUM	−0.55	0.33	4
MBC	−0.70	0.32	9
MLO	−0.67	0.36	6
NWR	−0.55	0.28	8
PSA	−0.66	0.39	6
SEY	−0.86	0.36	12
SMO	−0.68	0.29	7
SPO	−0.88	0.37	6
STM	−0.62	0.34	8
global average	−0.70	0.38	7

* σ is the standard deviation near 0 lag if there is no correlation.

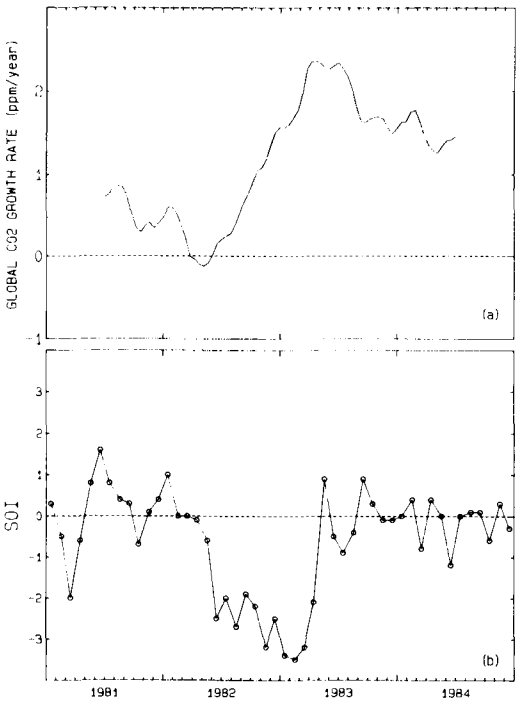

Fig. 11. (a) The globally averaged CO_2 growth rate determined from the GMCC flask network, 1981–84. (b) The southern oscillation index, 1981–84 (Climate Analysis Center, 1986).

Our results are consistent with previous studies of the relationship between the SOI and CO_2 growth rates. They found that low SOI is associated with higher CO_2 growth rates and that high SOI is associated with lower growth rates (see, for example, Bacastow, 1976; Bacastow et al., 1980; Keeling et al., 1985). If a connection between SOI and CO_2 growth rates had to be based solely on the measurements presented here, we could only call the correlation coefficients suggestive. To be conclusive we would require the correlation to hold up strongly during the next ENSO event.

The mechanism by which the global atmospheric CO_2 content is altered in connection with the southern oscillation is by no means clear, and several hypotheses have been proposed (see, for example, Bacastow, 1976; Newell and Weare, 1977; Machta et al., 1977; Bacastow et al., 1980; Ascencio-Parvy et al., 1984; Keeling and Revelle, 1985; Feely et al., 1987). A full discussion of the question is beyond the scope of this paper.

The mean growth rates for the period 1981 to 1984 for 17 sites were calculated by dividing the difference between the 1984 and 1981 annual means by 3 (Table 7). The statistical uncertainty of the mean growth rate is then

$$\sigma_G = 1/3^*(\sigma^2_{(84)} + \sigma^2_{(81)})^{\frac{1}{2}}. \quad (8)$$

The 4-year global mean growth rate calculated from these 17 sites is 1.22 ppm yr^{-1}, $\sigma = 0.01$ ppm yr^{-1}. The uncertainty of the global mean was calculated form the individual uncertainties, σ_G, according to the formula

$$\sigma_\mu = \left\{\frac{1}{\sum(1/\sigma_i^2)}\right\}^{\frac{1}{2}} \quad (9)$$

from Bevington (1969). This growth rate is lower than that observed over the past decade due to the effect of the 1982–83 ENSO event discussed above.

The 4-year mean growth rates are plotted versus latitude in Fig. 12. The most obvious feature in this plot is the high scatter relative to the mean compared to the statistical (1σ) uncertainty of the individual 4-year means. The growth rate at PSA appears to be low relative to SPO and AMS, which may be due to poor data quality at PSA in 1981 (see above). The growth rate at STM is also low relative

Table 7. *Mean CO_2 growth rate 1981–1984*

Site	Growth rate ppm yr^{-1}	σ_G
AMS	1.33	0.02
ASC	1.30	0.03
AVI	0.96	0.03
AZR	1.65	0.10
BRW	1.26	0.06
CBA	1.44	0.08
GMI	1.01	0.04
KEY	1.11	0.10
KUM	1.15	0.03
MBC	1.22	0.03
MLO	1.21	0.03
NWR	1.57	0.06
PSA	0.86	0.04
SEY	1.21	0.07
SMO	1.35	0.03
SPO	1.22	0.04
STM	0.92	0.05
global	1.22	0.01

The statistical uncertainties, σ_G, are defined in the text.

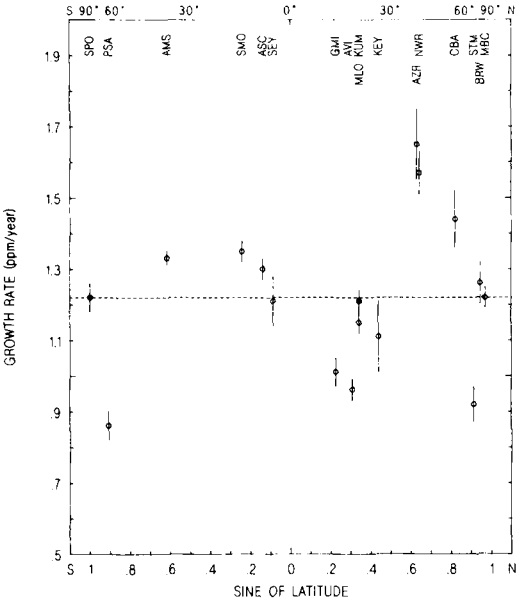

Fig. 12. Latitudinal variation of the 4-year mean CO_2 growth rates for 17 flask network sites. The error bars are the statistical uncertainties of the mean growth rates (see text and Table 7). The symbol for MLO is filled to distinguish it from KUM. The dashed line indicates the global mean growth rate calculated from the 17 sites for 1981–84.

to sites to the north and south of it. There is a suggestion of a pattern in the scatter of the growth rates with values greater than the mean in midlatitudes of the northern hemisphere (AZR, NWR) and growth rates lower than the mean in the northern hemisphere tropics (GMI, AVI). Since the mean growth rate due to the fossil fuel CO_2 source is expected to be the same at all sites, these results suggest that variations in regional scale non-fossil fuel sources and marine or biospheric sinks may be manifested temporarily in regionally different growth rates. The pattern in Fig. 12 could be caused by an increasing sink or a decreasing source in the northern hemisphere tropics acting in concert with an increasing source or decreasing sink in midlatitudes of the northern hemisphere. This scenario is consistent with formulations of the mechanism for the ENSO perturbation of CO_2 growth rates mentioned above. Mean growth rates from longer records would be expected to show little variation with latitude, but variations on shorter time scales, as observed here, may prove valuable in understanding the variability of regional scale sources and sinks.

5. Conclusion

Several features of the 1981–84 NOAA/GMCC flask network record have been analyzed using an objective statistical method. The 4-year mean north-to-south interhemispheric concentration difference was 3.1 ppm. Interannual variability of the meridional gradient was observed, particularly of the local CO_2 maximum normally found in the equatorial region. The observed decrease in this feature during 1982 may be related to the 1982–83 ENSO event. The latitudinal variation of the seasonality of CO_2 concentration is well defined in the northern hemisphere but is more variable and difficult to determine in the southern hemisphere. No evidence for trends in either the phase or amplitude of the seasonal cycle was found in the four years studied. The global atmospheric CO_2 concentration continued to increase but considerable spatial and temporal variation in the rate of increase was observed. The spatial and short-term temporal variability of the CO_2 growth rate is likely due to regional variations in CO_2 sinks and non-fossil fuel CO_2 sources. A significant long-term anomaly in the CO_2 growth rate was observed in association with the 1982–83 ENSO event. Low growth rates in 1982 were followed by high growth rates in early 1983. Growth rates in late 1983 and 1984 returned to values more typical of the period preceding the ENSO event. The flask network data clearly demonstrated the global extent of the ENSO related carbon cycle perturbation and the four years studied span the complete cycle of low and high growth rates associated with ENSO events.

The statistical uncertainties, due to residual random noise, associated with parameters derived from the data have been quantified. Annual and monthly means, the phase of the seasonal cycle in the northern hemisphere, and long-term growth rates are determined with relatively small uncertainties. The amplitude of the seasonality, the phase in the southern hemisphere, and short-term growth rates are determined with relatively large uncertainties. These uncertainties limit the amount and type of information that can be

extracted from a flask data record. For example, the ENSO effect is clear in the long-term CO_2 growth rate, but no significant ENSO effect on the amplitude or phase of the CO_2 seasonality was observed. If there is a biospheric CO_2 effect on seasonality associated with ENSO events, it is obscured by the noise in the data.

This study of an internally consistent, globally representative set of atmospheric CO_2 concentration measurements provides a detailed record of the atmospheric response to the combined effects of the global carbon cycle and anthropogenic and natural perturbations of that cycle. These results can be used to evaluate the estimates of sources, sinks, and fluxes of CO_2 in the atmosphere–ocean–biosphere system produced by carbon cycle models. This combination of models and measurements to constrain them will lead to a greater understanding of this complex system.

6. Acknowledgements

We gratefully acknowledge the individuals who have done a fine job in collecting thousands of air samples, often under difficult circumstances. We also appreciate the cooperation of the agencies listed in Table 1 and their representatives who have helped handle the logistics of the network. These contributions are essential to the success of this project. Finally, we thank J. Flueck for helpful discussions concerning the statistical analyses.

REFERENCES

Ascencio-Parvy, J. M., Gaudry, A. and Lambert, G. 1984. Year-to-year CO_2 variations at Amsterdam Island in 1980–83. *Geophys. Res. Lett. 11*, 1215–1217.

Bacastow, R. B. 1976. Modulation of atmospheric carbon dioxide by the Southern Oscillation. *Nature 261*, 116–118.

Bacastow, R. B. 1977. Influence of the Southern Oscillation on atmospheric carbon dioxide. In: *The fate of fossil fuel CO_2 in the oceans* (eds. N. R. Anderson and A. Malahoff). New York, USA. Plenum, 33–43.

Bacastow, R. B., Adams, J. A., Keeling, C. D., Moss, D. J. and Whorf, T. P. 1980. Atmospheric carbon dioxide, the Southern Oscillation, and the weak 1975 El Niño. *Science 210*, 66–68.

Bacastow, R. B., Keeling, C. D. and Whorf, T. P. 1985. Seasonal amplitude increase in atmospheric CO_2 concentration at Mauna Loa, Hawaii, 1959–82. *J. Geophys. Res. 90*, 10529–10540.

Bevington, P. R. 1969. *Data reduction and error analysis for the physical sciences*. New York, USA. McGraw-Hill, Inc., 336 pp.

Bortniak, J. C. 1981. The wind climatology of American Samoa. *NOAA Tech. Memo. ERL ARL-98*. NOAA Environ. Res. Lab., Boulder, Colo., USA, 67 pp.

Box, G. E. P. and Jenkins, G. M. 1976. *Time series analysis: forecasting and control*. San Francisco, Calif., USA. Holden-Day Inc., 575 pp.

Cleveland, W. S., Freeny, A. E. and Graedel, T. E. 1983. The seasonal component of atmospheric CO_2: Information from new approaches to the decomposition of seasonal time series. *J. Geophys. Res. 88*, 10934–10946.

Climate Analysis Center. 1986. *Climate diagnostics bulletin: March 1986*. NOAA/NWS Nat. Meteorol. Center, Washington, DC, USA.

Craven, P. and Wahba, G. 1979. Smoothing noisy data with spline functions. *Numer. Math. 31*, 377–403.

De Boor, C. 1978. *A practical guide to splines*. New York, USA. Springer-Verlag, 392 pp.

DOE, 1985a. *Projecting the climatic effects of increasing carbon dioxide* (DOE/ER-0237). US Department of Energy, Washington, DC, 381 pp.

DOE, 1985b. *Direct effects of increasing carbon dioxide on vegetation* (DOE/ER-0238). US Department of Energy, Washington, DC, 286 pp.

DOE, 1985c. *Glaciers, ice sheets, and sea level: Effect of a CO_2-induced climatic change* (DOE/ER/60235-1). US Department of Energy, Washington, DC. 330 pp.

Edmonds, J. A. and Reilly, J. M. 1985. Future global energy and carbon dioxide emissions. In: *Atmospheric carbon dioxide and the global carbon cycle* (ed. J. R. Trabalka) DOE/ERL-0239. US Department of Energy, Washington, DC, 215–245.

Enting, I. G. 1986. Potential problems with the use of least squares spline fits to filter CO_2 data. *J. Geophys. Res. 91*, 6668–6670.

Enting, I. G. 1987. The interannual variation in the seasonal cycle of carbon dioxide concentration at Mauna Loa. *J. Geophys. Res. 92*, 5497–5504.

EPA, 1983. *Projecting future sea level rise: Methodology, estimates to the year 2100, and research needs* (EPA 230-09-007). US Environmental Protection Agency, Washington, DC, 121 pp.

Feely, R. A., Gammon, R. H., Taft, B. A., Pullen, P. E., Waterman, L. S., Conway, T. J., Gendron, J. F. and Wisegarver, D. P. 1987. Distribution of chemical tracers in the eastern equatorial Pacific during and after the 1982–83 El Niño/Southern Oscillation event. *J. Geophys. Res. 92*, 6545–6558.

Fraser, P. J., Pearman, G. I. and Hyson, P. 1983. The global distribution of atmospheric carbon dioxide. 2. A review of provisional background observations, 1978–80. *J. Geophys. Res. 88*, 3591–3598.

Fung, I., Prentice, K., Matthews, E., Lerner, J. and Russell, G. 1983. Three-dimensional tracer model study of atmospheric CO_2: Response to seasonal exchanges with the terrestrial biosphere. *J. Geophys. Res. 88*, 1281–1294.

Gammon, R. H., Sundquist, E. T. and Fraser, P. J. 1985. History of carbon dioxide in the atmosphere. In: *Atmospheric carbon dioxide and the global carbon cycle* (ed. J. R. Trabalka) DOE/ER-0239. US Department of Energy, Washington, DC, 25–62.

Gaudry, A., Ascencio, J. M. and Lambert, G. 1983. Preliminary study of CO_2 variations at Amsterdam Island (Territoire des Terres Australes et Antarctiques Francaises). *J. Geophys. Res. 88*, 1323–1329.

Harris, J. M. and Nickerson, E. C. (eds.) 1984. *Geophysical monitoring for climatic change, no. 12. Summary Report 1983.* Environ. Res. Lab., US Dept. of Commerce, Boulder, Colo., 184 pp.

ISSCO, 1981. *DISSPLA version 9.0.* Integrated Software Systems Co., San Diego, Calif., USA.

Keeling, C. D., Bacastow, R. B., Bainbridge, A. E., Ekdahl, C. A., Guenther, P. R., Waterman, L. S. and Chin, J. F. S. 1976a. Atmospheric carbon dioxide variations at Mauna Loa Observatory, Hawaii. *Tellus 28*, 538–551.

Keeling, C. D., Adams, J. A., Ekdahl, C. A. and Guenther, P. R. 1976b. Atmospheric carbon dioxide variations at the South Pole. *Tellus 28*, 552–564.

Keeling, C. D., Whorf, T. P., Wong, C. S. and Bellegay, R. D. 1985. The concentration of atmospheric carbon dioxide at Ocean Weather Station P from 1969 to 1981. *J. Geophys. Res. 90*, 10511–10528.

Keeling, C. D. and Revelle, R. 1985. Effects of El Niño/Southern Oscillation on the atmospheric content of carbon dioxide. *Meteoritics 20*, 437–450.

Keeling, C. D. and Heimann, M. 1986. Meridional eddy diffusion model of the transport of atmospheric carbon dioxide. 2. Mean annual carbon cycle. *J. Geophys. Res. 91*, 7782–7796.

Komhyr, W. D., Waterman, L. S. and Taylor, W. R. 1983. Semiautomatic nondispersive infrared analyzer apparatus for CO_2 air sample analyses. *J. Geophys. Res. 88*, 1315 1322.

Komhyr, W. D., Gammon, R. H., Harris, T. B., Waterman, L. S., Conway, T. J., Taylor, W. R. and Thoning, K. W. 1985a. Global atmospheric CO_2 distribution and variations from 1968–82 NOAA/GMCC CO_2 flask sample data. *J. Geophys. Res. 90*, 5567–5596.

Komhyr, W. D., Harris, T. B. and Waterman, L. S. 1985b. Calibration of nondispersive infrared CO_2 analyzers with CO_2-in-air reference gases. *J. Atmos. and Oceanic Technol. 2*, 82–88.

Machta, L., Hanson, K. J. and Keeling, C. D. 1977. Atmospheric carbon dioxide and some interpretation. In: *The fate of fossil fuel CO_2 in the oceans* (eds. N. R. Anderson and A. Malahoff). New York, USA. Plenum, 131–143.

Mook, W. G., Koopmans, M., Carter, A. F. and Keeling, C. D. 1983. Seasonal, latitudinal, and secular variations in the abundance and isotopic ratios of atmospheric carbon dioxide. 1. Results from land stations. *J. Geophys. Res. 88*, 10915–10933.

Newell, R. E. and Weare, B. C. 1977. A relationship between atmospheric carbon dioxide and Pacific sea surface temperature. *Geophys. Res. Lett. 4*, 1–2.

Nickerson, E. C. (ed.) 1986. *Geophysical monitoring for climatic change, no. 14. Summary Report 1985.* Environ. Res. Lab., US Dept. of Commerce, Boulder, Colo., 146 pp.

Oeschger, H. and Heimann, M. 1983. Uncertainties of predictions of future atmospheric CO_2 concentrations. *J. Geophys. Res. 88*, 1258–1262.

Pearman, G. I., Hyson, P. and Fraser, P. J. 1983. The global distribution of atmospheric carbon dioxide. 1. Aspects of observations and modeling. *J. Geophys. Res. 88*, 3581–3590.

Pearman, G. I. and Beardsmore, D. J. 1984. Atmospheric carbon dioxide measurements in the Australian region: ten years of aircraft data. *Tellus 36B*, 1–24.

Pearman, G. I. and Hyson, P. 1986. Global transport and inter-reservoir exchange of carbon dioxide with particular reference to stable isotopic distributions. *J. Atmos. Chem. 4*, 81–124.

Ramanathan, V., Cicerone, R. J., Singh, H. B. and Kiehl, J. T. 1985. Trace gas trends and their potential role in climate change. *J. Geophys. Res. 90*, 5547–5566.

Reinsch, C. H. 1967. Smoothing by spline functions. *Numer. Math. 10*, 177–183.

Rotty, R. M. 1983. Distribution of and changes in industrial carbon dioxide production. *J. Geophys. Res. 88*, 1301–1308.

Rotty, R. M. 1987. A look at 1983 CO_2 emissions from fossil fuels (with preliminary data for 1984). *Tellus 39B*, 203–208.

Steele, L. P., Fraser, P. J., Rasmussen, R. A., Khalil, M. A. K., Conway, T. J., Crawford, A. J., Gammon, R. H., Masarie, K. A. and Thoning, K. W. 1987. The global distribution of methane in the troposphere. *J. Atmos. Chem. 5*, 125–171.

Tanaka, M., Nakazawa, T. and Aoki, S. 1983. High quality measurements of the concentration of atmospheric carbon dioxide. *J. Meteorol. Soc. Japan 61*, 678–685.

Tanaka, M., Nakazawa, T. and Aoki, S. 1987a. Seasonal and meridional variations of atmospheric carbon dioxide in the lower troposphere of the northern and southern hemispheres. *Tellus 39B*, 29–41.

Tanaka, M., Nakazawa, T., Shiobara, M., Ohshima, H., Aoki, S., Kawaguchi, S., Yamanouchi, T., Makino, Y. and Morayama, H. 1987b. Variations of atmospheric carbon dioxide concentration at Syowa

Station (69°00′S, 39°35′E), Antarctica. *Tellus 39B*, 72–79.

Thompson, M. L., Enting, I. G., Pearman, G. I. and Hyson, P. 1986. Interannual variation of atmospheric CO_2 concentration. *J. Atmos. Chem. 4*, 125–155.

Thoning, K. W., Tans, P., Conway, T. J. and Waterman, L. S. 1987. NOAA/GMCC calibrations of CO_2-in-air reference gases: 1979–85. *NOAA Tech. Memo.* (ERL ARL-150). Environ. Res. Lab., Boulder, Colo., 63 pp.